

Metadata of the article that will be visualized in OnlineFirst

ArticleTitle	Experimental and Theoretical Correlation of Modulated Architectures of β -Ag ₂ MoO ₄ Microcrystals: Effect of Different Synthesis Routes on the Morphology, Optical, Colorimetric, and Photocatalytic Properties	
Article Sub-Title		
Article CopyRight	The Author(s), under exclusive licence to Springer Science+Business Media, LLC, part of Springer Nature (This will be the copyright line in the final PDF)	
Journal Name	Journal of Inorganic and Organometallic Polymers and Materials	
Corresponding Author	FamilyName	Cavalcante
	Particle	
	Given Name	L. S.
	Suffix	
	Division	GERATEC-CETEM-PPGQ
	Organization	Universidade Estadual do Piauí
	Address	Rua: João Cabral, N. 2231, P.O. Box 381, Teresina, PI, 64002-150, Brazil
	Division	Programa de Pós-Graduação em Ciências e Engenharia dos Materiais-PPGCEM
	Organization	Universidade Federal do Piauí
	Address	Teresina, PI, 64049-550, Brazil
	Phone	
	Fax	
	Email	laeciosc@gmail.com
	URL	
	ORCID	
Author	FamilyName	Lopes
	Particle	
	Given Name	F. H. P.
	Suffix	
	Division	GERATEC-CETEM-PPGQ
	Organization	Universidade Estadual do Piauí
	Address	Rua: João Cabral, N. 2231, P.O. Box 381, Teresina, PI, 64002-150, Brazil
	Phone	
	Fax	
	Email	
	URL	
	ORCID	
Author	FamilyName	Noieto
	Particle	
	Given Name	L. F. G.
	Suffix	
	Division	Programa de Pós-Graduação em Química-PPGQ
	Organization	Universidade Federal do Piauí
	Address	Teresina, PI, 64049-550, Brazil
	Phone	
	Fax	
	Email	
	URL	
	ORCID	
Author	FamilyName	Vieira
	Particle	
	Given Name	V. E. M.
	Suffix	
	Division	Programa de Pós-Graduação em Química-PPGQ
	Organization	Universidade Federal do Piauí
	Address	Teresina, PI, 64049-550, Brazil
	Phone	
	Fax	
	Email	
	URL	
	ORCID	

Author	FamilyName	Sousa
	Particle	de
	Given Name	P. B.
	Suffix	
	Division	Programa de Pós-Graduação em Ciências e Engenharia dos Materiais-PPGCEM
	Organization	Universidade Federal do Piauí
	Address	Teresina, PI, 64049-550, Brazil
	Phone	
	Fax	
	Email	
	URL	
	ORCID	
Author	FamilyName	Jucá
	Particle	
	Given Name	A. C. S.
	Suffix	
	Division	GERATEC-CETEM-PPGQ
	Organization	Universidade Estadual do Piauí
	Address	Rua: João Cabral, N. 2231, P.O. Box 381, Teresina, PI, 64002-150, Brazil
	Phone	
	Fax	
	Email	
	URL	
	ORCID	
Author	FamilyName	Oliveira
	Particle	
	Given Name	Y. L.
	Suffix	
	Division	Programa de Pós-Graduação em Ciências e Engenharia dos Materiais-PPGCEM
	Organization	Universidade Federal do Piauí
	Address	Teresina, PI, 64049-550, Brazil
	Phone	
	Fax	
	Email	
	URL	
	ORCID	
Author	FamilyName	Costa
	Particle	
	Given Name	K. R. B. S.
	Suffix	
	Division	Programa de Pós-Graduação em Ciências e Engenharia dos Materiais-PPGCEM
	Organization	Universidade Federal do Piauí
	Address	Teresina, PI, 64049-550, Brazil
	Phone	
	Fax	
	Email	
	URL	
	ORCID	

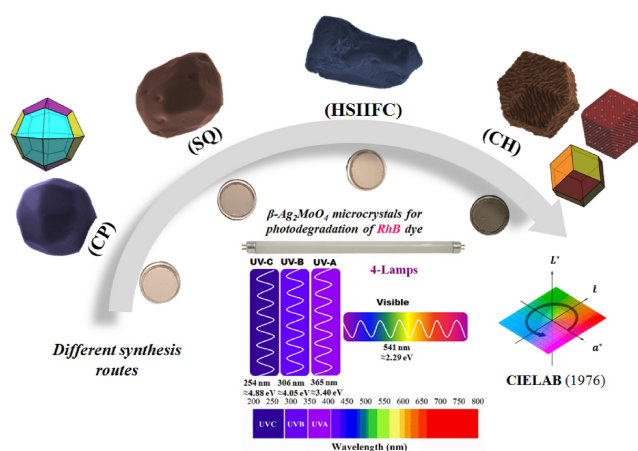
Author	FamilyName	Almeida
	Particle	
	Given Name	M. A. P.
	Suffix	
	Division	PPGQ, PPGAero, Centro de Ciências Exatas e Tecnologia
	Organization	Universidade Federal do Maranhão-CCET
	Address	São Luís, MA, 65085-580, Brazil
	Phone	
	Fax	
	Email	
	URL	
	ORCID	

Author	FamilyName	Gouveia
	Particle	
	Given Name	A. F.
	Suffix	
	Division	Department of Analytical and Physical Chemistry
	Organization	University Jaume I
	Address	12071, Castelló, Spain
	Phone	
	Fax	
	Email	
	URL	
	ORCID	

Schedule	Received	17 Aug 2022
	Revised	
	Accepted	1 Nov 2022

Abstract In this paper, the effect of different synthesis methods, such as controlled precipitation (CP), sonochemical (SC), hot solution ion injection with fast cooling and conventional hydrothermal (CH) in obtaining beta-disilver molybdate ($\beta\text{-Ag}_2\text{MoO}_4$) are explained in details. X-ray diffraction patterns, Rietveld refinement data, cluster modeling, micro-Raman, and Fourier transform infrared spectroscopies confirmed that all $\beta\text{-Ag}_2\text{MoO}_4$ crystals have a spinel-like cubic structure, space group ($Fd\bar{3}m$), and symmetry point group (O_h^7). Field emission scanning electron microscopy (FE-SEM) images showed that through different synthetic routes, it is possible to obtain monophasic crystals, such as regular/irregular polyhedrons (cubes, cuboctahedron, trapezohedron, rhombic dodecahedron), potatoes, and non-uniform. The crystal shape observed experimentally was modeled based on Rietveld refinement data and FE-SEM images obtained by KrystalShaper. First-principles quantum mechanical calculations based on density functional theory were employed to modulate the surfaces of the material and to obtain their surface energy (E_{surf}) values. From these E_{surf} values in association with the Wulff construction, the evolution of the crystals shape was achieved correlating with the experimental results when different synthesis methods are used. Ultraviolet–Visible (UV–Vis) spectroscopy measurements in absorbance mode showed three main absorptions (280, 310, and 340 nm), while the UV–Vis analyses in diffuse reflectance mode showed a tail of energy absorption in the UV spectrum range (3.25 eV and 3.3 eV). The quantitative data from the colorimetric analysis indicated that the $\beta\text{-Ag}_2\text{MoO}_4$ crystals are desirable for developing inorganic pigments with a beige to brown shade. Photocatalytic assays were performed using four lamps: UV-C, UV-B, UV-A, and visible light. The $\beta\text{-Ag}_2\text{MoO}_4$ crystals prepared by the CP method showed a higher degradation rate at 85.12% for the rhodamine B dye solution under 240 min exposure to UV-C light.

Graphical Abstract:



Keywords (separated by '- Synthesis methods - β -Ag₂MoO₄ - Crystal shape - Surface energies - Colorimetry - Photocatalysis
)

Footnote Information



2 **Experimental and Theoretical Correlation of Modulated Architectures**
3 **of β -Ag₂MoO₄ Microcrystals: Effect of Different Synthesis Routes**
4 **on the Morphology, Optical, Colorimetric, and Photocatalytic**
5 **Properties**

6 F. H. P. Lopes¹ · L. F. G. Noletto² · V. E. M. Vieira² · P. B. de Sousa³ · A. C. S. Jucá¹ · Y. L. Oliveira³ · K. R. B. S. Costa³ ·
7 M. A. P. Almeida⁴ · A. F. Gouveia⁵ · L. S. Cavalcante^{1,3}

8 Received: 17 August 2022 / Accepted: 1 November 2022

9 © The Author(s), under exclusive licence to Springer Science+Business Media, LLC, part of Springer Nature 2022

10 **Abstract**

11 In this paper, the effect of different synthesis methods, such as controlled precipitation (CP), sonochemical (SC), hot solu-
12 tion ion injection with fast cooling, and conventional hydrothermal (CH) in obtaining beta-disilver molybdate (β -Ag₂MoO₄)
13 are explained in details. X-ray diffraction patterns, Rietveld refinement data, cluster modeling, micro-Raman, and Fourier
14 transform infrared spectroscopies confirmed that all β -Ag₂MoO₄ crystals have a spinel-like cubic structure, space group (*Fd*
15 $\bar{3}m$), and symmetry point group (*O_h⁷*). Field emission scanning electron microscopy (FE-SEM) images showed that through
16 different synthetic routes, it is possible to obtain monophasic crystals, such as regular/irregular polyhedrons (cubes, cuboc-
17 tahedron, trapezohedron, rhombic dodecahedron), potatoes, and non-uniform. The crystal shape observed experimentally
18 was modeled based on Rietveld refinement data and FE-SEM images obtained by KrystalShaper. First-principles quantum
19 mechanical calculations based on density functional theory were employed to modulate the surfaces of the material and to
20 obtain their surface energy (*E_{surf}*) values. From these *E_{surf}* values in association with the Wulff construction, the evolution
21 of the crystals shape was achieved correlating with the experimental results when different synthesis methods are used.
22 Ultraviolet–Visible (UV–Vis) spectroscopy measurements in absorbance mode showed three main absorptions (280, 310,
23 and 340 nm), while the UV–Vis analyses in diffuse reflectance mode showed a tail of energy absorption in the UV spectrum
24 range (3.25 eV and 3.3 eV). The quantitative data from the colorimetric analysis indicated that the β -Ag₂MoO₄ crystals
25 are desirable for developing inorganic pigments with a beige to brown shade. Photocatalytic assays were performed using
26 four lamps: UV-C, UV-B, UV-A, and visible light. The β -Ag₂MoO₄ crystals prepared by the CP method showed a higher
27 degradation rate at 85.12% for the rhodamine B dye solution under 240 min exposure to UV-C light.

A1 ✉ L. S. Cavalcante
A2 laeciosc@gmail.com

A3 ¹ GERATEC-CETEM-PPGQ, Universidade Estadual
A4 do Piauí, Rua: João Cabral, N. 2231, P.O. Box 381, Teresina,
A5 PI 64002-150, Brazil

A6 ² Programa de Pós-Graduação em Química–PPGQ,
A7 Universidade Federal do Piauí, Teresina, PI 64049-550,
A8 Brazil

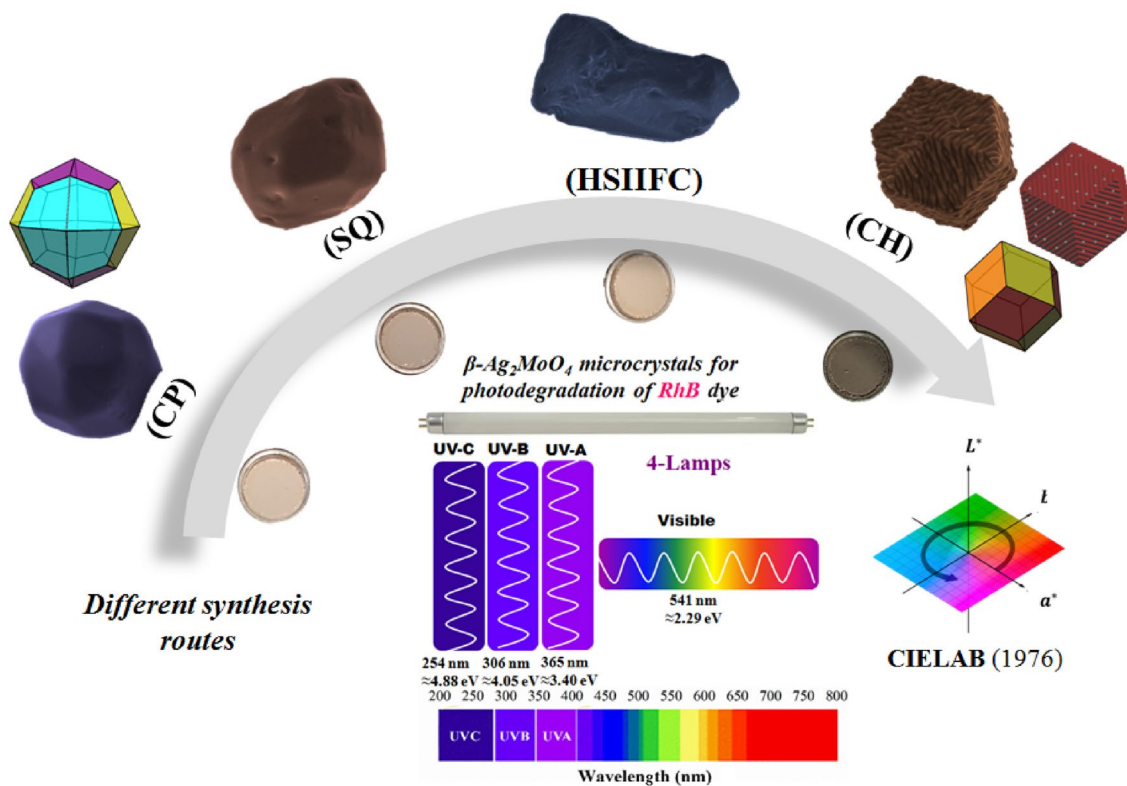
A9 ³ Programa de Pós-Graduação em Ciências e Engenharia
A10 dos Materiais-PPGCEM, Universidade Federal do Piauí,
A11 Teresina, PI 64049-550, Brazil

A12 ⁴ PPGQ, PPGAero, Centro de Ciências Exatas e Tecnologia,
A13 Universidade Federal do Maranhão-CCET, São Luís,
A14 MA 65085-580, Brazil

A15 ⁵ Department of Analytical and Physical Chemistry, University
A16 Jaume I, 12071 Castelló, Spain

28 Graphical Abstract

29



30

31 **Keywords** Synthesis methods · $\beta\text{-Ag}_2\text{MoO}_4$ · Crystal shape · Surface energies · Colorimetry · Photocatalysis32 **1 Introduction**

33 Mixed-anion compounds, perovskite-type lanthanum
 34 ferrite, bismuth-based materials, and materials oxides
 35 exhibit excellent electronic properties, such as photoca-
 36 talysis, photoelectrochemistry, photoluminescence, pho-
 37 tocatalytic water splitting, battery electrodes, thermoelec-
 38 tric, and sensors by the virtual of the anionic diversity in
 39 ionic radius, electronegativities, and polarizability [1–5].
 40 Moreover, metal molybdates are significant inorganic
 41 structures that depend on the type of lattice-formed ion;
 42 two structural organizations can be found, scheelite-type,
 43 for large bivalent cation (ionic radius > 0.99 Å such Ca,
 44 Ba, Pb, Sr) and wolframite-type when smaller bivalent
 45 cation such (ionic radius < 0.77 Å) Fe, Mn, Co, Ni, Mg
 46 are found [6]. These scheelite and wolframite oxides have
 47 attracted much interest due to potential applications such
 48 as scintillators, optical devices, sensors, lasers, optical
 49 fibers, and catalytic [7–9]. In particular, the molybdates
 50 with the specific molecular formula $X_2\text{MoO}_4$, $X = \text{Li}^+$,
 51 Tl^+ , and Ag^+ . In particular, the use of silver ions (Ag^+) as
 52 monovalent cation leads to the formation of alpha-disilver

molybdate ($\alpha\text{-Ag}_2\text{MoO}_4$) crystals or beta-disilver molyb-
 53 date ($\beta\text{-Ag}_2\text{MoO}_4$) crystals has been reported very recently
 54 in the literature in different papers [10–17].
 55

56 In the specific case of $\alpha\text{-Ag}_2\text{MoO}_4$ crystals with a meta-
 57 stable tetragonal structure, obtaining requires quirky and
 58 extremely sensible conditions for obtaining the pure phase,
 59 which requires reagents such as 3-bis(2-pyridyl)pyrazine
 60 as doping or the use of high hydrostatic pressures. On the
 61 other hand, the cubic structure of the species, related to the
 62 $\beta\text{-Ag}_2\text{MoO}_4$ crystals, can be easily obtained at room tem-
 63 perature, with prohibited band energy (E_{gap}) ranging from
 64 3.2 to 3.4 eV, which has attracted more attention due to its
 65 stability and rapid synthesis in the laboratory [18–23].

66 The first work reported in the literature by Wyckoff [24]
 67 on the obtention of $\beta\text{-Ag}_2\text{MoO}_4$ crystals employs the tra-
 68 ditional methodology of solid-state reaction or mixture
 69 of oxides. However, this synthesis method can generate a
 70 large amount of non-uniform oxide, large grains, and vari-
 71 ous porous. This rudimentary method, for many years, has
 72 been described as simple and very conventional, which is
 73 based on the mechanical mixture of oxides, carbonates, or
 74 start salts, with subsequent heat treatment above 1000 °C
 75 [25–27,].

Alternatively, other synthetic methods have been presented in the preparation of $\beta\text{-Ag}_2\text{MoO}_4$ crystals, such as precipitation with calcination at high temperatures [25] and crystal growth, using the process called “Czochralski” [27]. However, these methods required long processing times, high temperatures, and sophisticated equipment with high maintenance costs. Furthermore, these methodologies induced the formation of deleterious or secondary phases and produced crystals with irregular shapes and sizes and inhomogeneous granulometry.

Therefore, based on the several negative points described above, significant technological advances were recently pointed out, and through the use of new synthesis methods and the optimization of those already existing for the preparation of $\beta\text{-Ag}_2\text{MoO}_4$ crystals have been described, the most reported in the literature as synthetic methodologies are precipitation (P) [27, 28], sonochemical (SC) [29], hot solution ion injection with fast cooling (HSIIFC) [30], conventional hydrothermal (CH) [31, 32], and microwave-hydrothermal (MH) [33].

In the last five years, significant advances and improvements in the synthesis routes have possibilities significant advances in the obtention of $\beta\text{-Ag}_2\text{MoO}_4$ crystals, which allowed improving their electronic properties, in particular their catalytic property, due to obtaining crystals with high purity [34], structural changes under high pressure [35], theoretical and experimental study on the electronic structure, highly energetic facets and photoluminescent properties of $\beta\text{-Ag}_2\text{MoO}_4$ microcrystals with different sizes and shapes prepared by the MH method [36]. Ng et al. [37] obtained $\alpha\text{-}\beta\text{-Ag}_2\text{MoO}_4$ crystals with uniform and well-defined shapes through the controlled precipitation (CP) method and optimizing experimental parameters, such as reagent concentration, addition mode, and temperature. These factors enabled its use as a catalyst in the degradation processes of organic pollutants, using advanced oxidative processes (AOPs), specifically in heterogeneous photocatalysis [38]. In another paper, Chen et al. [28] prepared $\beta\text{-Ag}_2\text{MoO}_4/\text{BiVO}_4$ heterojunctions using the simple precipitation method and tested the photocatalytic activity of these materials on the degradation of rhodamine B (RhB) dye and tetracycline hydrochloride, obtaining a photocatalytic performance of about of 92.6% in the degradation of these pollutants. Fabbro et al. [39] prepared $\beta\text{-Ag}_2\text{MoO}_4$ microcrystals by precipitation method with different solvents (water, ethanol, and ammonia) in various pH ranges and investigated their optical antifungal properties.

Recently, Ferreira et al. [40] investigated the influence of the pH of the reaction medium on the $\beta\text{-Ag}_2\text{MoO}_4$ obtained by the SC method, obtaining materials with different phases and particles with asymmetric shapes of nanorods (at acidic pH) and without a defined form (at basic pH) of micrometric order. The catalytic property of

these powders was evaluated in the photocatalytic degradation of the methylene blue (MB) dye under ultraviolet light (UV) irradiation. The catalysts showed promise for the photodegradation of MB dye, mineralizing about 95% of its concentration after 35 min of UV light irradiation. A recent study reported in the literature [41] has investigated the photocatalytic degradation of ethylene in H_2O and CO_2 under UV-A light irradiation using $\beta\text{-Ag}_2\text{MoO}_4/g\text{-C}_3\text{N}_4$ composites synthesized by a modified hydrothermal method.

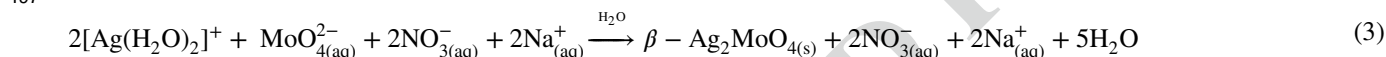
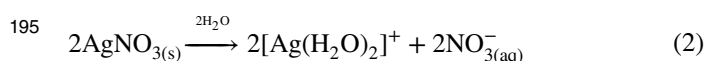
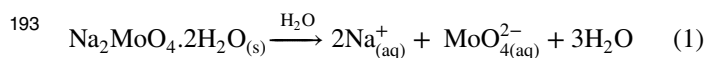
In all the literature, only one paper [30] reported the preparation of $\beta\text{-Ag}_2\text{MoO}_4$ microcrystals synthesized by the ion’s injection method in a hot solution at 90 °C in 1 min with fast cooling by immersion in an ice bath or HSIIFC method. In this paper, Cunha et al. [30] have employed this synthesis route to prepare microcrystals of silver and zinc molybdate [$\beta\text{-(Ag}_{2-2x}\text{Zn}_x\text{)MoO}_4$] with the following concentrations ($x = 0; 0.01; \text{ and } 0.02$), the materials obtained show a photodegradation rate of approximately 99.99% of the RhB dye concentration under 120 min of UV-C light.

It is worth mentioning that, to date, there are no studies reported in the literature on the morphology, optical, colorimetric, and photocatalytic properties of $\beta\text{-Ag}_2\text{MoO}_4$ microcrystals prepared by four different synthesis methods. However, the influence of preparation methods on the properties of semiconductor materials has already been discussed in the research. For example, the work reported by Oliveira et al. [41, 42] prepared nickel tungstate (NiWO_4) and cobalt tungstate (CoWO_4) using co-precipitation and polymeric precursors methods. These two methods promoted significant changes in structural, optical, morphological, and colorimetric properties, showing favorable responses for their use as inorganic pigments for both materials and supercapacitive for CoWO_4 nanocrystals [42].

Therefore, because of the above and in a different way, we have focused in prepared the $\beta\text{-Ag}_2\text{MoO}_4$ microcrystals obtained by four synthesis methods such as (I) CP, (II) SC, (III) HSIIFC, and (IV) CH. The products obtained were characterized by X-ray diffraction (XRD), Rietveld refinements, micro-Raman spectroscopy, Fourier transform infrared spectroscopy, field emission scanning electron microscopy (FE-SEM), and ultraviolet–visible (UV–Vis) spectroscopy. Moreover, we combined first-principles calculations, at density functional theory (DFT) level, with the Wulff construction to find suitable crystals with a specific shape and to achieved the morphology evolution by using different synthesis methods. Finally, a quantitative analysis of the colorimetric coordinates and the evaluation of the photocatalytic activity of these $\beta\text{-Ag}_2\text{MoO}_4$ microcrystals in the degradation of the cationic organic RhB dye was carried out using UV-C, UV-B, UV-A, and visible lamps.

182 **2 Experimental and Theoretical Details**183 **2.1 Chemicals Reactions and Synthesis Methods**

184 For the synthesis of β - Ag_2MoO_4 microcrystals, we have
 185 employed four synthetic routes, which are described in short
 186 as CP, SC, HSIIFC, and CH, with the following precursors:
 187 sodium molybdate dihydrate ($\text{Na}_2\text{MoO}_4 \cdot 2\text{H}_2\text{O}$; 99.5% purity;
 188 Sigma-Aldrich®) at a concentration of 1 mmol, silver nitrate
 189 (AgNO_3 ; 99.0% purity, Sigma-Aldrich®) with 2 mmols. The
 190 solvent was deionized (DI) water (H_2O) with 200 mL. The
 191 chemical reactions of precipitation of β - Ag_2MoO_4 micro-
 192 crystals are presented by Eqs. (1–3) below:



198 After the reaction time, for each methodology used, pre-
 199 cipitates were subjected to 10 washing cycles in an Eppen-
 200 dorf® centrifuge (model 5804R) at 8000 rotations per min-
 201 ute (RPM) for 10 min each process to remove spectator ions.
 202 Finally, the materials oxide obtained were dried at 65 °C
 203 for 10 h in a muffle furnace (model EDG3000/3P) with a
 204 heating rate of 5 °C /min. The following topics provide a
 205 detailed description of the methodologies used to prepare
 206 β - Ag_2MoO_4 crystals.

207 **2.1.1 Synthesis of β - Ag_2MoO_4 Crystals by the CP**
 208 **Method**

209 Initially, 1 mmol of $\text{Na}_2\text{MoO}_4 \cdot 2\text{H}_2\text{O}$ was dissolved with
 210 150 mL of DI H_2O in a beaker with a maximum capacity of
 211 250 mL, and this solution was maintained and heated using
 212 a hot plate 90 °C under constant stirring at 380 RPM. Then,
 213 2 mmol of AgNO_3 was dissolved with 50 mL of DI H_2O in
 214 a beaker with a capacity of 250 mL under the same previ-
 215 ous temperature and stirring conditions. Then the second
 216 solution containing the diaquasilver(I) as $[\text{Ag}(\text{H}_2\text{O})_2]^+$
 217 complex cations and NO_3^- ions were transferred to a volumetric
 218 burette. Finally, this solution was slowly dripped into the
 219 solution containing the molybdate MoO_4^{2-} complex anions,
 220 making a total reaction time of 3 h.

221 **2.1.2 Synthesis of β - Ag_2MoO_4 Crystals by the SC**
 222 **Method**

223 In a typical synthesis, 1 mmol of $\text{Na}_2\text{MoO}_4 \cdot 2\text{H}_2\text{O}$ and
 224 2 mmol of AgNO_3 salts were dissolved separately in 100 mL
 225 of DI H_2O until complete solubilization. Subsequently, the
 226 solution containing the $[\text{Ag}(\text{H}_2\text{O})_2]^+$ complex cations and
 227 NO_3^- ions was dripped into the MoO_4^{2-} complex anions in
 228 an ultrasound bath (Branson CPX-1800 model with a fre-
 229 quency of 42 kHz). After that, this mixture was kept under
 230 the sonication process at 45 °C for 3 h. After this time, a
 231 beige precipitate is observed.

232 **2.1.3 Synthesis of β - Ag_2MoO_4 Crystals by the HSIIFC**
 233 **Method**

234 In this type of HSIIFC synthesis, 1 mmol of $\text{Na}_2\text{MoO}_4 \cdot 2\text{H}_2\text{O}$
 235 was dissolved in 50 mL of DI H_2O and briefly heated on a
 236 plate at 90 °C under constant stirring at 380 RPM, solution

237 A. Then, 2 mmol AgNO_3 was dissolved in 50 mL of DI H_2O
 238 under the same temperature and stirring conditions, solu-
 239 tion B. Then, the $[\text{Ag}(\text{H}_2\text{O})_2]^+$ complex cations and NO_3^-
 240 ions were sucked into a syringe and quickly injected into the
 241 aqueous solution containing the MoO_4^{2-} complex anions and
 242 Na^+ ions. Immediately, the formation of a white suspension
 243 was observed and quickly transferred to a plastic beaker con-
 244 taining 100 mL of DI H_2O at 2 °C, which was later placed in
 245 the refrigerator, remaining at rest for 24 h. After that time, a
 246 beige precipitate is observed.

247 **2.1.4 Synthesis of β - Ag_2MoO_4 Crystals by the CH**
 248 **Method**

249 The conventional hydrothermal (CH) synthesis is per-
 250 formed initially with the dissolution of 1 mmol of the
 251 $\text{Na}_2\text{MoO}_4 \cdot 2\text{H}_2\text{O}$ salt in 100 mL of DI H_2O . Then, 2 mmol of
 252 the AgNO_3 was dissolved in 100 mL of DI H_2O . At the next
 253 stage, these solutions were mixed into the red screw-top bot-
 254 tle (borosilicate 3.3, Germany) from DURAN®GL 45 with
 255 high-temperature resistance, making a total solution volume
 256 of 200 mL. Then, this high-strength glass bottle was closed
 257 and transferred to a glycerin bath thermal and maintained at
 258 a constant temperature of 90 °C under stirring at 380 RPM
 259 for 3 h. Finally, we noted a formation of a large amount of
 260 brown-colored precipitates at the bottom of the flask.

2.2 Characterizations

The pure β - Ag_2MoO_4 crystals synthesized by these different methodologies were structurally characterized by X-ray diffraction patterns (XRD) through an X-ray Diffractometer (Rigaku, Japan, model DMax2500PC), operated under conditions of 40 kV and 60 mA. The radiation used for the measurements was Cu-K α (wavelength $\lambda = 1.5406 \text{ \AA}$) with a scan rate of $0.02^\circ/\text{min}$ in the 2θ range from 10° to 110° for routine measurements from the Rietveld Refinement method [44]. The powder diffractograms were compared to diffraction patterns, agreeing with the Inorganic Crystal Structure Data (ICSD), card N $^\circ$ 36,187. XRD diffractograms were refined by the Rietveld method, using a routine conducted in the 2θ range from 10° to 110° with a sweep speed of $1^\circ/\text{min}$ and a step of 0.02° in ReX software version 0.9.2 [45]. These unit cells of crystals are modeled through the Rietveld refinement data using the software VESTA (Visualization for Electronic and Structural Analysis $^\circ$) version 3.5.8 [46]. Micro-Raman spectra at room temperature were performed using a Bruker Senterra model spectrometer with an Olympus BX50 microscope with a charge-coupled device (CCD) as a detector. The excitation source was a laser, which provided a wavelength of 532 nm, and output power of 5 mW. The spectral resolution of the spectrometer was set to 3 cm^{-1} , sweeping in the range from 50 to 1550 cm^{-1} . Fourier transform-infrared spectroscopy (FT-IR) measurements using a Bomem-Michelson spectrometer, model MB-102, programmed in transmittance mode. Pressed the sample holder used in this test KBr pellets. The spectral region analyzed covered a range from 400 to 4000 cm^{-1} . The morphological characteristics were obtained in a field emission scanning electron microscope (FE-SEM) brand Jeol JSM7100F with an electron acceleration voltage of 5 kV in secondary electron detection (SED) mode. Optical properties were investigated using diffuse ultraviolet–visible (UV–Vis) reflectance spectra obtained on a Shimadzu Scientific Instruments spectrophotometer (model UV-2600, Japan) in diffuse reflectance mode. The staining of β - Ag_2MoO_4 crystals was analyzed in an 8 mm portable digital colorimeter model WR-10QC and brand (FRU $^\circ$) in a standard observer CIE 10° , measuring the range of luminosity (L^*) 0–100, and through the color difference formula: ΔE^*a^*b in the CIELAB color space, established by the International Commission on Illumination (CIE) in 1976 [47, 48].

2.3 Theoretical Methodology

First-principles calculations of the β - Ag_2MoO_4 surfaces were carried out within the periodic DFT framework using the Perdew–Burke–Ernzerhof (PBE) functional [49, 50] in the Vienna ab initio Simulation Package VASP.5.2.2 [52,

53]. More details about the methodology can be found in the previous work reported by us [53].

The (100), (110), (111), and (112) surfaces models of β - Ag_2MoO_4 were constructed from optimized bulk structure and, after full optimization of the models, it was calculated their surface energies (E_{surf}). The E_{surf} is defined as the total energy per repeating cell of the slab minus the total energy for the same number of atoms in the perfect crystal (bulk), divided by the surface area per repeating cell for the two sides of the slab, as shown in Eq. (4):

$$E_{\text{surf}} = \frac{(E_{\text{slab}} - nE_{\text{bulk}})}{2A} \quad (4)$$

The calculation of E_{surf} values employing the Wulff construction results in a crystal shape that depends only on the ratios between the values of surface energies and symmetry point group [54, 55]. The Wulff theorem [59] provides a simple relation between the E_{surf} of the each (hkl) plane and its distance (d) in the normal direction from the center of the crystallite.

The energy profiles connected the different morphologies were also calculated by using the polyhedron energy (E_{pol}) values, as proposed by Macedo et al. [57], using the following Eq. 5:

$$E_{\text{pol}} = \sum_i C_i \times E_{\text{surf}}^i \quad (5)$$

where C_i is the area of the surface by the total area of the polyhedron ($C_i = A^i / A^{\text{pol}}$), and E_{surf}^i is the surface energy value of the corresponding surface (i). The calculated energy profiles are capable of offering a morphological evolution that can be occurs during a synthetic process.

2.4 Photocatalytic Assays

The photocatalytic properties of β - Ag_2MoO_4 crystals, synthesized by the CP, SC, HSIIFC, and CH methods, were investigated in the degradation of the aqueous solution of the RhB dye ($\text{C}_{28}\text{H}_{31}\text{ClN}_2\text{O}_3$, CAS: 81889, with 95% purity, Sigma-Aldrich) at a concentration of $1 \times 10^{-5} \text{ mol. L}^{-1}$, under UV-C, UV-B, UV-A, and Vis-light irradiation in an exposure time of 240 min. For each test, 50 mg of the catalysts were used for a volume of 50 mL of the dye solution. This final solution was homogenized in an ultrasonic bath (model M1800, BRANSON $^\circ$, 40 kHz, 70 W) for 10 min. After this time, this solution was subjected to photocatalytic systems consisting of four lamps of different UV-lights and visible-light absorption ranges, namely: UV-C light (OSRAM $^\circ$ brand, 15 W, $\lambda_{\text{max}} = 254 \text{ nm} \approx 4.88 \text{ eV}$), UV-B (USHIO $^\circ$ brand, 15 W, $\lambda_{\text{max}} = 306 \text{ nm} \approx 4.05 \text{ eV}$), UV-A light (OZLI $^\circ$ brand, 15 W, $\lambda_{\text{max}} = 365 \text{ nm} \approx 3.40 \text{ eV}$) and visible light (OSRAM brand $^\circ$, 15 W, $\lambda_{\text{max}} = 541 \text{ nm} \approx$

2.29 eV). It is worth noting that these lamps were positioned approximately 45 cm from the solution. Before starting the irradiation in each system, Keep the suspensions for 30 min under stirring in the dark to reach adsorption–desorption equilibrium between the liquid and solid phases. After that, 2.2 mL aliquots were collected at interphases of 10, 20, and 40 min, making a total test time of 240 min. Next, aliquots were centrifuged (6000 RPM for 20 min) to separate the catalysts from the liquid phase. The variations in maximum absorption bands of the RhB dye solution were monitored during the photocatalytic tests at the characteristic wavelength of the color of this dye, approximately ($\lambda_{\text{max}} = 554 \text{ nm}$); for this, a UV-2600 spectrophotometer (Shimadzu®, Japan). The catalytic efficiency to photolysis and photocatalysis was determined through Eq. (6):

$$\text{Catalyst efficiency } [\beta - \text{Ag}_2\text{MoO}_4 \text{ crystals } M(\%)] = \frac{C_0 - C_t}{C_0} \times 100 \quad (6)$$

where C_0 is the concentration of the RhB dye solution at the beginning; C_t is the concentration of the RhB dye solution at time t ; M the synthesis methods used (CP, SC, HSIIFC, and CH methods).

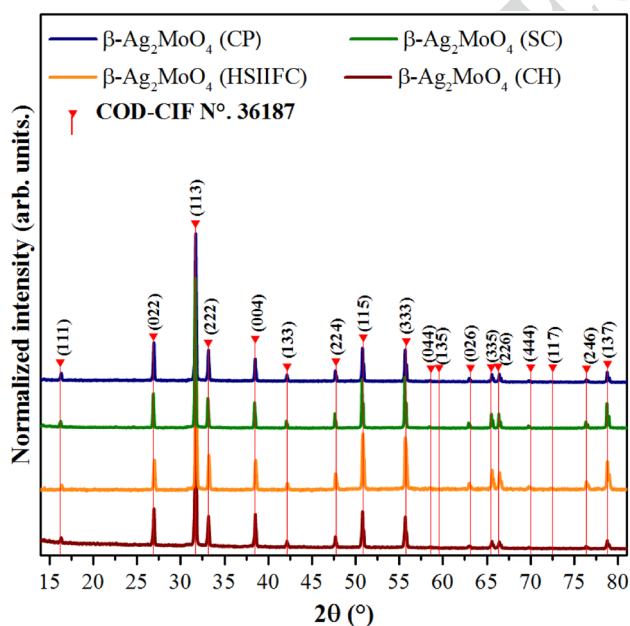


Fig. 1 XRD patterns normalized for $\beta\text{-Ag}_2\text{MoO}_4$ crystals synthesized by the CP, HSIIFC, SC, and CH synthesis methods. The vertical lines (l) indicate the respective positions and intensities found on the COD-CIF card N° 36,187, corresponding to the $\beta\text{-Ag}_2\text{MoO}_4$ phase and spinel-like cubic structure

3 Results and Discussion

3.1 X-ray Diffraction (XRD) Analyses

Performed XRD analysis to verify the long-range order, dis- order degree, and crystal lattice periodicity for $\beta\text{-Ag}_2\text{MoO}_4$ crystals synthesized by CP, HSIIFC, SC, and CH methods are exhibited in Fig. 1.

Based on the analysis of Fig. 1, it is noted that all microcrystals present XRD patterns, which are correctly indexed to beta (β)-phase related to spinel-like cubic structure, with lattice parameters ($a = b = c = 9.6 \text{ \AA}$), space group ($Fd\bar{3}m$) and symmetry of point group (O_h^7) [24, 58]. In each peak of the diffractograms, the Miller indices (hkl) of the crystal-line planes corresponding to each of them are shown. These diffraction peaks are refined and well-defined, indicating that the materials synthesized by the different methodologies have a long-range degree of crystallinity. No diffraction peaks associated with silver oxide (Ag_2O) or reduced silver particles (Ag^0) were observed, confirming the effectiveness of the methods used to obtain pure $\beta\text{-Ag}_2\text{MoO}_4$ crystals. Furthermore, the positions of the diffraction peaks arranged in the diffractogram, as seen in Fig. 1, agree with the results described in the Inorganic Crystal Structure Data (ICSD) database, card N°. 36,187, and with the literature [24, 59].

3.2 Rietveld Refinement Analyses

Figures 2a–d show the structural refinement plots for $\beta\text{-Ag}_2\text{MoO}_4$ microcrystals obtained by CP, SC, HSIIFC, and CH methods. The Rietveld refinement method made it possible to calculate the experimental lattice parameters (atomic positions), the unit cell volume, and the quality indicators for the microcrystals. For this, we have employed ReX software version 0.9.2 [45]. The refinement method developed by Hugo Rietveld [42] has proved to be an essential tool for analyzing crystalline samples. It allows the quantification of data in the XRD patterns and their comparison with information from crystallographic fixtures of reported materials. In addition, they are making it possible to extract experimental details, namely: the lattice parameters (a , b , c), internal angles (α , β , and γ) that are vectors that describe the curves of a crystal, unit cell volume (V), observed parameters (Y_{Obs}), calculated parameters (Y_{Calc}) for the residual line profile ($Y_{\text{Obs}} - Y_{\text{Calc}}$), R -parameters (R_{exp} , R_{wp} , and R_b), χ^2 (χ^2) and Goodness of Fit (GoF) that describe the refinement quality [60].

As displayed in Figs. 2a–d, the Rietveld structural refinement method again confirmed the spinel-like cubic structure for the $\beta\text{-Ag}_2\text{MoO}_4$ microcrystals, synthesized differently. The formation of secondary phases was not identified. These

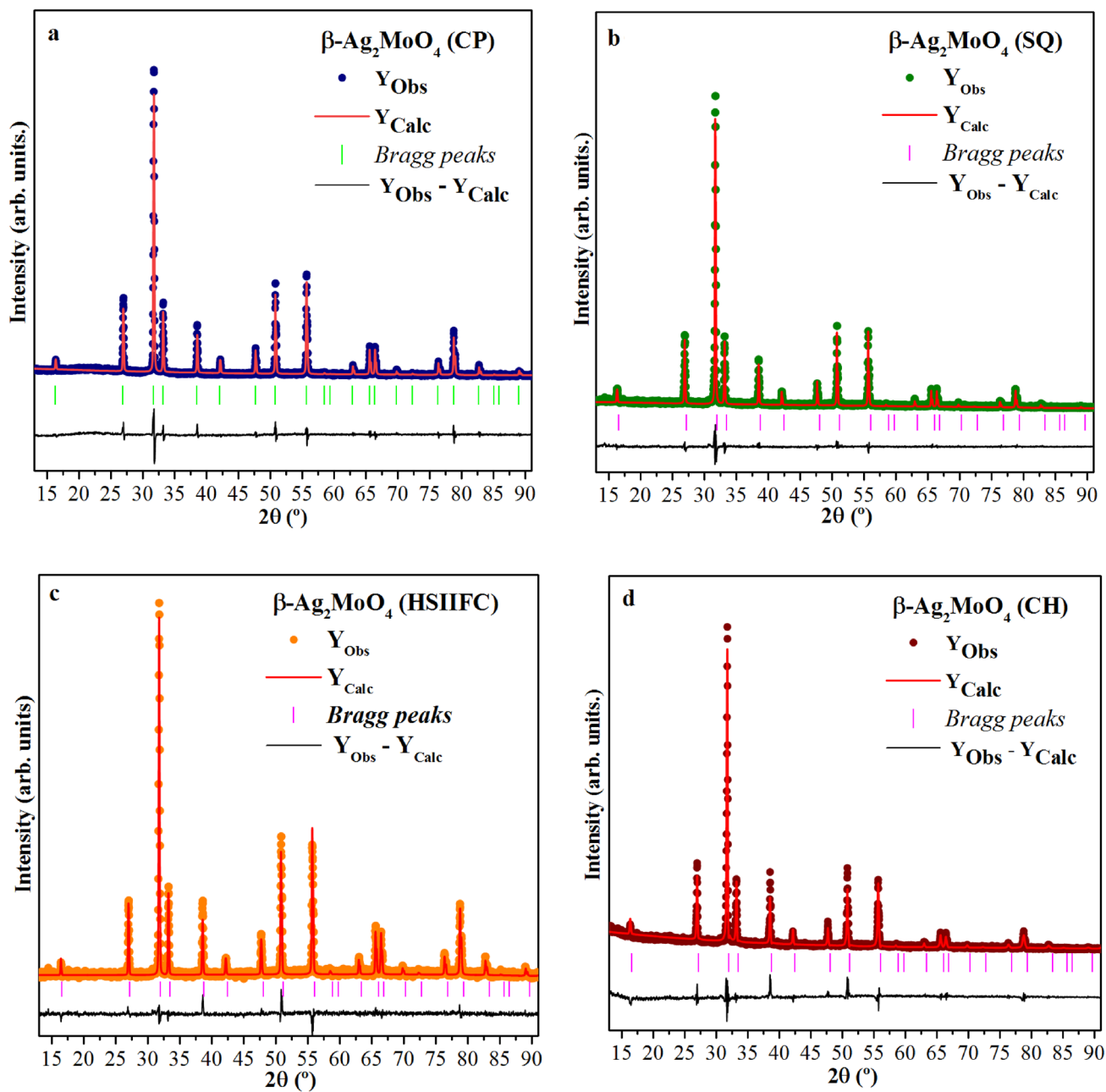


Fig. 2 a–d: Rietveld refinement of XRD diffractograms for $\beta\text{-Ag}_2\text{MoO}_4$ crystals synthesized by the **a** CP, **b** SC, **c** HSIIFC, and **d** CH synthesis methods

426 results agree with those seen in the XRD patterns and the
 427 information extracted from the ICSD card No. 36187 [24]. It
 428 is also possible to observe that the adjustment curves of Y_{Obs}
 429 and Y_{Calc} overlap, and the residual line profile ($\text{Y}_{\text{Obs}} - \text{Y}_{\text{Calc}}$)
 430 approaches a straight line; this indicates that the refinement
 431 of the crystal structures was efficient [61].

432 Tables 1(a–d) display the Rietveld refinement data
 433 obtained from $\beta\text{-Ag}_2\text{MoO}_4$ microcrystals. In these tables,
 434 the values of the adjustment parameters, or static indica-
 435 tors of refinement, R_p , R_{wp} , R_{ex} , and GOF are in the range

436 considered for a cubic structure with Bravais lattice, where:
 437 ($a = b = c$) and ($\alpha = \beta = \gamma = 90^\circ$), evidencing a good quality
 438 of refinement [60, 61].

439 It is also noted that these different methods of $\beta\text{-Ag}_2\text{MoO}_4$
 440 synthesis produce microcrystals with different lattice param-
 441 eters and unit cell volumes. For example, the $\beta\text{-Ag}_2\text{MoO}_4$
 442 microcrystals made by the CP method showed a lattice
 443 parameter ($a = 9.257781 \text{ \AA}$), while the $\beta\text{-Ag}_2\text{MoO}_4$ micro-
 444 crystals prepared by the other methods present the follow-
 445 ing lattices parameters values such as ($a = 9.260089 \text{ \AA}$) for

Table 1 Lattice parameters, unit cell volume, atomic coordinates, and local occupation, obtained by Rietveld refinement data for β - Ag_2MoO_4 microcrystals synthesized by the (a) CP, (b) HSIIFC, (c) SC, and (d) CH synthesis methods

a) β - Ag_2MoO_4 -CP method						
Átomos	Wyckoff	Site	x	y	z	U_{iso}
Ag	16d	0.– 3 m	0.625	0.625	0.625	0.062616
Mo	8a	– 43 m	0.0	0.0	0.0	0.047788
O	32e	0.3 m	0.350236	0.350236	0.350236	0.050264
b) β - Ag_2MoO_4 -SC method						
Ag	16d	0.– 3 m	0.625	0.625	0.625	0.104475
Mo	8a	– 43 m	0.0	0.0	0.0	0.092989
O	32e	0.3 m	0.353186	0.353186	0.353186	0.101848
c) β - Ag_2MoO_4 -FCHSII method						
Ag	16d	0.– 3 m	0.625	0.625	0.625	0.056612
Mo	8a	– 43 m	0.0	0.0	0.0	0.045665
O	32e	0.3 m	0.357521	0.357521	0.357521	0.056612
d) β - Ag_2MoO_4 -CH method						
Ag	16d	0.– 3 m	0.625	0.625	0.625	0.056612
Mo	8a	– 43 m	0.0	0.0	0.0	0.055207
O	32e	0.3 m	0.357521	0.357521	0.357521	0.02658

a) $a=9.257781$ Å; $b=9.257781$ Å; $c=9.257781$ Å; $\alpha=90^\circ$; $\beta=90^\circ$; $\gamma=90^\circ$; Unit Cell Volume: 793.4521 Å³; $\rho=6.29$ g/cm³; $\mu=161.41$ cm²/g; $R_p=9.6575\%$; $R_{wp}=12.5381\%$; $R_{exp}=7.3833\%$; $\chi^2=2.883804$; GoF=1.698176. b) $a=9.260089$ Å; $b=9.260089$ Å; $c=9.260089$ Å; $\alpha=90^\circ$; $\beta=90^\circ$; $\gamma=90^\circ$; Unit Cell Volume: 794.046 Å³; $\rho=6.28$ g/cm³; $\mu=162.20$ cm²/g; $R_p=10.1345\%$; $R_{wp}=13.65\%$; $R_{exp}=10.8119\%$; $\chi^2=1.59389615$; GoF=1.262496. c) $a=9.235101$ Å; $b=9.235101$ Å; $c=9.235101$ Å; $\alpha=90^\circ$; $\beta=90^\circ$; $\gamma=90^\circ$; Unit Cell Volume: 787.635 Å³; $\rho=6.34$ g/cm³; $\mu=157.72$ cm²/g; $R_p=8.5633\%$; $R_{wp}=11.0357\%$; $R_{exp}=9.5585\%$; $\chi^2=1.332962$; GoF=1.154544. d) $a=9.317389$ Å; $b=9.317389$ Å; $c=9.317389$ Å; $\alpha=90^\circ$; $\beta=90^\circ$; $\gamma=90^\circ$; Unit Cell Volume: 808.877 Å³; $\rho=6.28$ g/cm³; $\mu=161.31$ cm²/g; $R_p=14.3049\%$; $R_{wp}=19.0334\%$; $R_{exp}=10.2384\%$; $\chi^2=3.455937$; GoF=1.859015

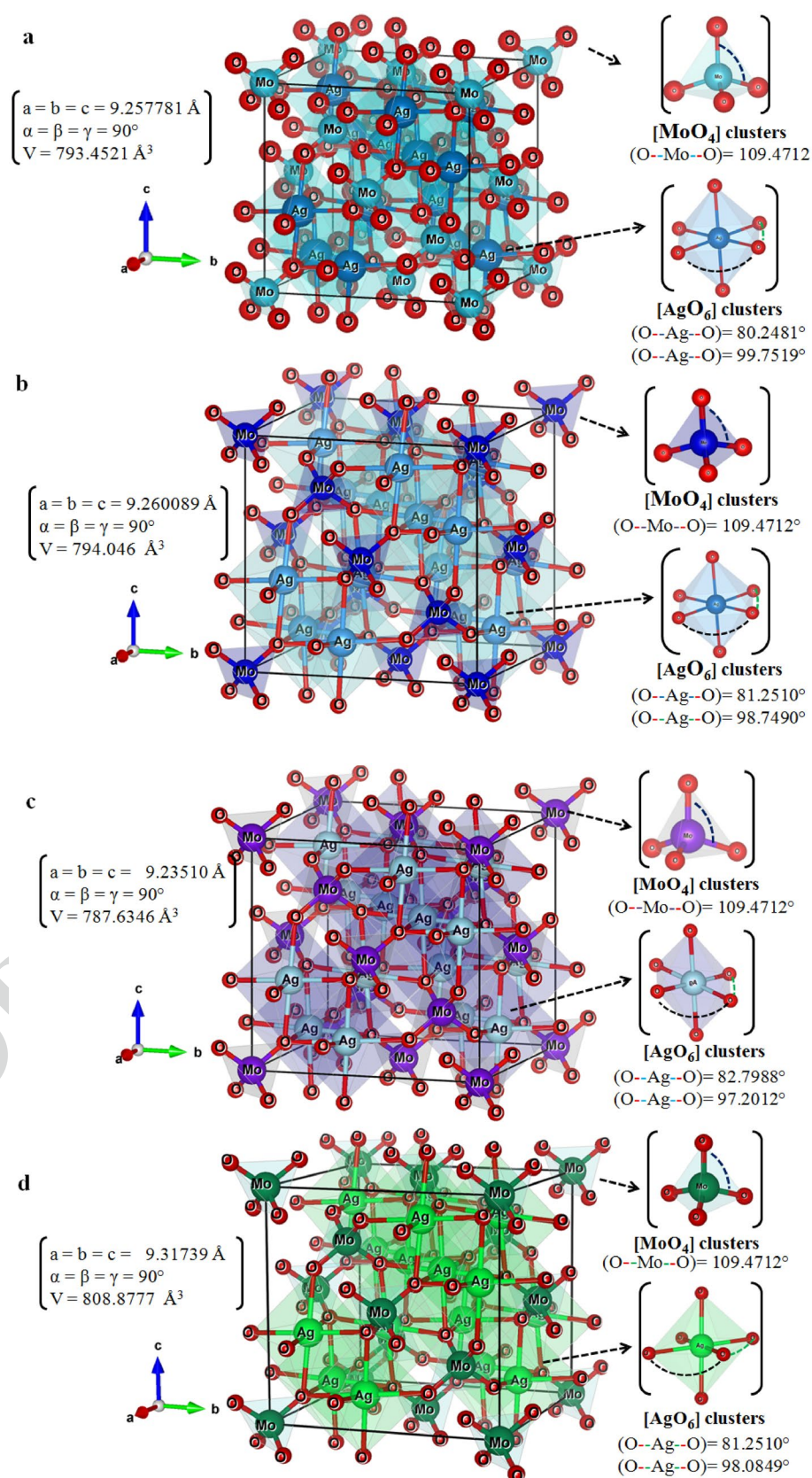
446 SC, ($a=9.235101$ Å) for HSIIFC and ($a=9.317389$ Å) for
 447 CH. Unit cell volume results followed the same trend, where
 448 β - Ag_2MoO_4 microcrystals made by the CP method exhib-
 449 ited the value (793.4521 Å³), followed by those prepared
 450 by the other synthesis methods such a (794.046 Å³) for SC,
 451 (787.635 Å³) for HSIIFC, and (808.877 Å³) for CH. On the
 452 other hand, the relative positions of the O atoms showed
 453 slight variations in positions, while the Ag and Mo atoms
 454 remain fixed in their Wyckoff positions in the cubic lattice
 455 [24]. This information indicates distorted octahedral [AgO_6]
 456 clusters and undistorted tetrahedral [MoO_4] clusters in the
 457 spinel-like cubic structure. These differences in the lattice
 458 parameters and unit cell volume may be related to different
 459 distortions in the crystal lattice caused by residual stresses
 460 induced by the preparation conditions and processing times
 461 in the methodologies used [62]. These new observations
 462 demonstrate that pristine β - Ag_2MoO_4 microcrystals with
 463 naturally isotropic growth can be modified depending on
 464 the synthesis methodology employed.

3.3 Schematic Representation of Unit Cells for β - Ag_2MoO_4 Microcrystals

The data of lattice parameters and atomic positions obtained in the Rietveld refinement, Tables 1(a–d), and using the VESTA software (version 3.5.8, 64 bits for Windows) [39, 46], made it possible to model the unit cells of β - Ag_2MoO_4 microcrystals prepared by different methodologies, as shown in Fig. 3a–d.

Given the analysis of Fig. 3, one can confirm the spinel-like cubic structure with $Fd\bar{3}m$ space group and eight molecular formulas per unit cell ($Z=8$) for these microcrystals [34] as identified in XRD patterns and Rietveld refinement. For all unit cells of the β - Ag_2MoO_4 microcrystals, the Ag atoms are coordinated to 6 oxygen atoms (O) atoms, giving rise to distorted octahedral [AgO_6] clusters with two different bond angles between the Ag and O atom (O–Ag–O) in the horizontal plane (x, y) of the center of these octahedra, forming polyhedral that have a symmetry group (O_h) with six vertices, eight faces, and Twelve edges. However, the molybdenum atoms (Mo) are coordinated by four O atoms, promoting the formation of undistorted tetrahedral [MoO_4]

Fig. 3 a–d: Schematic representation of the unit cells of β - Ag_2MoO_4 microcrystals prepared by the **a** CP, **b** SC, **c** HSIIFC, and **d** CH synthesis methods



486 clusters with equal bond angles (O–Mo–O) that are related
 487 to the symmetry group (T_d) with four vertices, four faces,
 488 and six edges [34, 47, 48]. Furthermore, the analysis of
 489 Fig. 3a–d reveals that the different experimental conditions
 490 for the synthesis of β -(Ag_2MoO_4) microcrystals were able
 491 to promote slight variations in their crystal structure, such
 492 as chemical bonds and O–Mo–O bond angles of distorted
 493 octahedral [AgO_6] clusters remain the same.

494 3.4 Raman Spectroscopy Analyses

495 The Raman spectroscopy technique was used to confirm
 496 the short-distance organization and symmetry between the
 497 clusters of β - Ag_2MoO_4 microcrystals synthesized by the
 498 methods: CP, SC, HSIIFC, and CH, according to literature
 499 and group theory calculations [64, 65], β - Ag_2MoO_4 micro-
 500 crystals with a spinel-like cubic structure, space group ($Fd\bar{3}m$),
 501 point group symmetry (O_h^h), and eight molecules per cell
 502 unit ($Z=8$), exhibit 17 vibrational modes Acoustic + Optical
 503 (Raman and active-infrared/ $A_{1g} + 2A_{2u} + E_g + 2E_u + T_{1g} + 4$
 504 $T_{1u} + 3T_{2g} + 2T_{2u}$). Of these ways, only four were detected
 505 in this article, located in the region from 200 to 1100 cm^{-1} ,
 506 as illustrated in Fig. 4.

507 According to Fig. 4, the β - Ag_2MoO_4 microcrystals syn-
 508 thesized by CP, SC, and HSIIFC methods present intense and
 509 well-defined Raman modes, indicating these microcrystals
 510 are structurally ordered at a short range. Furthermore, those
 511 synthesized by the PC method showed the greater intensity

of their active Raman modes, indicating the production of
 materials with a more significant structural organization,
 short-range ordering, and more excellent crystallinity than
 the others. However, unlike the microcrystals made by the
 CH method, they exhibited a lower intensity of these modes,
 confirming the presence of defects in their crystal structure.
 In addition, no active modes related to secondary phases
 were observed, corroborating the information reported in
 the XRD patterns and the Rietveld refinement data, Fig. 1
 and Fig. 2a–d, respectively.

The first E_g mode, located in the region from 278 to
 283 cm^{-1} , is associated with the symmetrical bending of
 vibrations in the O and Mo bonds ($\Leftarrow \Leftarrow \text{O} \leftarrow \text{Mo} \rightarrow \text{O} \Rightarrow \Rightarrow$)
 of the tetrahedral [MoO_4] clusters [64], as well as the vibra-
 tions of the external structure of the octahedral [AgO_6] clus-
 ters [52, 53]. The second mode, T_{2g} , seen in the region from
 354 to 358 cm^{-1} , is attributed to the symmetrical bending
 mode caused by torsional vibrations in the bonds between
 O and Mo ($\Leftarrow \text{O} \rightarrow \text{Mo} \rightarrow \text{O} \Leftarrow$) of the tetrahedral [MoO_4]
 clusters [64, 65]. The third T_{2g} mode, located in the region
 of 761 to 766 cm^{-1} , is due to antisymmetric stretching and
 vibrations in the O and Mo bonds ($\swarrow \swarrow \text{O} \leftarrow \text{Mo} \rightarrow \text{O} \nearrow \nearrow$)
 of the undistorted tetrahedral [MoO_4] clusters. Finally, the
 last A_{1g} mode at approximately 873 to 878 cm^{-1} is related
 to symmetrical elongation ($\nu_1(\text{Ag})$) due to vibrations in the
 O and Mo bonds ($\leftarrow \text{O} \leftarrow \text{Mo} \rightarrow \text{O} \rightarrow$) in the undistorted
 tetrahedral [MoO_4] clusters [65]. The experimental posi-
 tions of the active modes in the Raman spectrum for the
 β - Ag_2MoO_4 microcrystals prepared by the CP, SC, HSIIFC,
 and CH methodologies, are shown in Table 2.

A detailed analysis of the results contained in Table 2
 confirms that these different methods promote some slight
 variations in the relative positions, corresponding to the
 active Raman modes, which are caused by distortions or
 changes in the size of the bonds (O–Mo–O, O–Ag–O),
 changes in the interaction forces involving the undistorted
 tetrahedral [MoO_4] clusters \leftrightarrow distorted octahedral [AgO_6]
 clusters and the presence of structural disorder in the crystal
 lattice [34, 64, 65], as evidenced in the Rietveld refinement
 analyses.

552 3.5 Fourier Transform Infrared (FTIR) Spectroscopy 553 Analyses

Infrared spectroscopy was performed to identify the vibra-
 tion frequencies of the bonds of atoms in β - Ag_2MoO_4 micro-
 crystals prepared by different methods. The β - Ag_2MoO_4
 microcrystals exhibit 10 vibrational modes in the IR spec-
 trum (the $2A_{2u}$, $2E_u$, and $2T_{2u}$, which are considered acous-
 tic vibration modes or inactive IR modes, and the $4T_{1u}$
 modes, which are active in IR). However, the four active IR
 modes can detect only one in the measured region (400 to

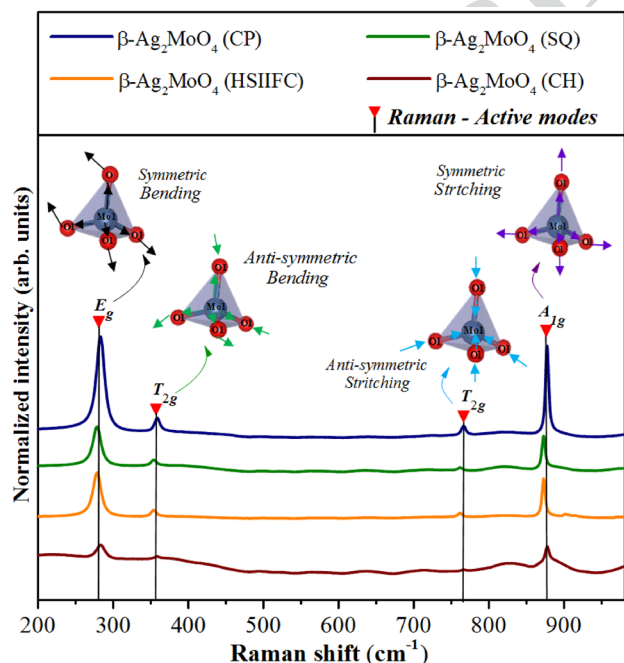
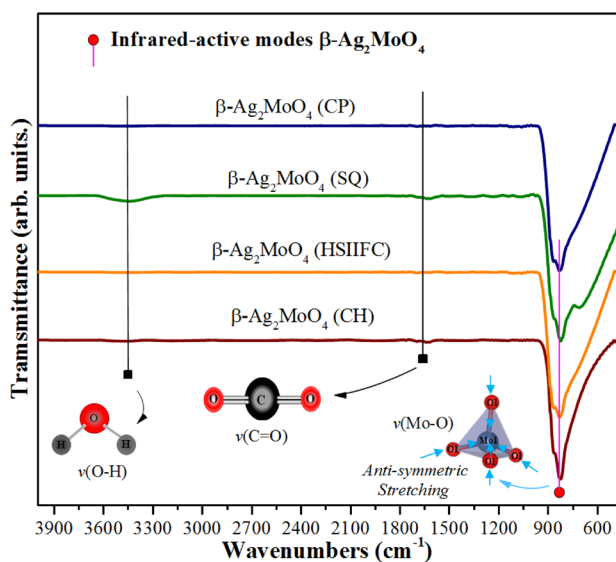


Fig. 4 Raman spectra of 7 β - Ag_2MoO_4 microcrystals prepared by CP, HSIIFC, SC, and HC methods

Table 2 Relative positions of the four experimental active-modes Raman for the β - Ag_2MoO_4 crystals were obtained by the CP, HSIIFC, SC, and CH synthesis methods

Raman active vibrational modes	Types of synthesis methods				Active- Raman Modes	Active- Raman Modes
	β - Ag_2MoO_4 - CP method	β - Ag_2MoO_4 - SC method	β - Ag_2MoO_4 - FCHSII method	β - Ag_2MoO_4 - CH method	Literature Ref [25] β - Ag_2MoO_4 -crystals	Literature Ref [28] β - Ag_2MoO_4 - crystals
E_g	283 cm^{-1}	278 cm^{-1}	278 cm^{-1}	283 cm^{-1}	277 cm^{-1}	278.5 cm^{-1}
T_{2g}	358 cm^{-1}	354 cm^{-1}	354 cm^{-1}	358 cm^{-1}	353 cm^{-1}	354.5 cm^{-1}
T_{2g}	766 cm^{-1}	762 cm^{-1}	761 \mathbf{cm}^{-1}	766 cm^{-1}	761 cm^{-1}	761.5 cm^{-1}
A_{1g}	878 cm^{-1}	873 cm^{-1}	873 cm^{-1}	878 cm^{-1}	872 cm^{-1}	873.5 cm^{-1}

References: [25]; [28]

**Fig. 5** FTIR spectra in the range from 4,000 to 500 cm^{-1} of β - Ag_2MoO_4 microcrystals were obtained by CP, HSIIFC, SC, and CH synthesis methods**Table 3** T_{1u} mode vibration frequencies are relative positions for β - Ag_2MoO_4 crystals obtained by CP, HSIIFC, SC, and CH synthesis methods

Infrared active vibrational modes	Types of synthesis methods			
	β - Ag_2MoO_4 - CP method	β - Ag_2MoO_4 - SC method	β - Ag_2MoO_4 - FCHSII method	β - Ag_2MoO_4 - CH method
T_{1u}	832/868 cm^{-1}	824/865 cm^{-1}	832/868 cm^{-1}	824/865/ cm^{-1}

562 1500 cm^{-1}); due to limitations in the IR equipment used in
563 this work, this mode is exhibited in Fig. 5.

564 The analysis of the FTIR spectra, Fig. 5, reveals that
565 β - Ag_2MoO_4 microcrystals prepared by CP, SC, HSIIFC,
566 and CH methods show a characteristic active mode of IR,

around 820 to 870 cm^{-1} , which is attributed to antisymmetric stretching of the O and Mo bonds ($\leftarrow \text{O} \leftarrow \text{Mo} \leftarrow \text{O} \leftarrow$)/ ($\rightarrow \text{O} \rightarrow \text{Mo} \rightarrow \text{O} \rightarrow$) within the distorted tetrahedral $[\text{MoO}_4]$ clusters [66–68]. Bands in these regions are typical in molybdenum oxide-based materials [66–69]. In addition, small bands of IR absorption are also observed in the middle area of 1,000 to 4000 cm^{-1} , which are associated with the presence of carbon dioxide (CO_2) and water (H_2O) from the room's humidity atmosphere. For example, the small band around the 1651 cm^{-1} region is related to the asymmetric and symmetrical $\nu(\text{C}=\text{O})$ stretching modes of CO_2 molecules. Moreover, the absorption band located at 3451 cm^{-1} is due to stretching vibrations $\nu(\text{O}-\text{H})$ of H_2O adsorbed on the surface of β - Ag_2MoO_4 microcrystals [34]. Table 3 shows the relative positions of the T_{1u} mode vibration frequencies for these microcrystals.

Different methodologies to prepare these microcrystals promoted small displacements in the active mode IV detected relative positions. This fact may be related to differences in the average size of the crystals obtained, distortions in the O–Mo–O/O–Ag–O bonds promoted during the synthesis, forces of interaction between distorted octahedral $[\text{AgO}_6]$ clusters/undistorted tetrahedral $[\text{MoO}_4]$ clusters, and different degrees of disorder-structural order in the short-range into the cubic lattice [34, 66, 67].

3.6 Field Emission Scanning Electron Microscopy (FE-SEM) Images Analyses

FE-SEM images analyzes were performed to verify the shape, average crystal size, and growth type of β - Ag_2MoO_4 microcrystals prepared using CP, SC, HSIIFC, and CH methods. Figures 6a–p show the FE-SEM images for β - Ag_2MoO_4 microcrystals synthesized by the different methods.

FE-SEM images analysis displayed in Figs. 6a–p confirms that the employment of different methods made it possible to obtain varied morphologies for the β - Ag_2MoO_4 microcrystals, such as some irregular shapes and also regular polyhedral-like shapes with well-defined facets ascribed to

604 cubes, cuboctahedron, truncated cuboctahedron, and convex
605 crystals with high-index facets for CP synthesis method, as
606 shown in Figs. 6a–d. These $\beta\text{-Ag}_2\text{MoO}_4$ microcrystals have
607 shapes with sizes ranging from 1.18 to 4.43 μm and an average
608 crystal size of approximately 2.8 mm.

609 The initial growth of first $\beta\text{-Ag}_2\text{MoO}_4$ precipitates or
610 nucleation seeds is related to the effect of electrostatic
611 attraction force between or interactions of Coulombic nature
612 between the cationic complex related to diaquasilver(I)
613 $[\text{Ag}(\text{H}_2\text{O})_2]^+$ and anionic complex ascribed to molybdate
614 solvated by water molecules $[\text{MoO}_4]^{2-} \dots x.\text{H}_2\text{O}$. In this
615 way, the initial precipitation of this solid oxide depends on
616 a competition between lattice energy crystal and stability of
617 solvation sphere solvation, including entropy effects related
618 to changes in the solvent structure. Therefore, due to the
619 high difference in electronic density between $[\text{Ag}(\text{H}_2\text{O})_2]^+$
620 and $[\text{MoO}_4]^{2-} \dots x.\text{H}_2\text{O}$ complexes, a strong electrostatic
621 attraction occurs between these ions, which results in the
622 formation of the first $\beta\text{-Ag}_2\text{MoO}_4$ precipitates or nucleation
623 seeds, which grow through Ostwald Ripening process [30].
624 These two processes induce a random aggregation between
625 the small particles due to the increase in effective collisions,
626 which results in several irregular crystals.

627 The small $\beta\text{-Ag}_2\text{MoO}_4$ crystals we have identified as
628 cube-like related to regular polyhedron, which are formed
629 by the one set of plans of the $\{100\}$ family and exhibit
630 six square faces, as illustrated by the insertion in Fig. 6a.
631 Moreover, these crystals grow during the CP synthesis,
632 and the facets numbers are increased to cuboctahedron-like
633 $\beta\text{-Ag}_2\text{MoO}_4$ microcrystals ascribed to regular polyhedron,
634 which are formed by the two sets of planes of the $\{100\}$
635 and $\{111\}$ families and exhibit six square faces, and eight
636 triangle faces, as shown in insertion at Fig. 6a. The convex
637 crystals with high-index facets are obtained at the final state
638 growth of $\beta\text{-Ag}_2\text{MoO}_4$ microcrystals prepared by the CP
639 method. These $\beta\text{-Ag}_2\text{MoO}_4$ crystals we have described as
640 trapezohedron-like and designed as irregular polyhedron;
641 this crystal shape is composed of twenty-four trapezoidal
642 faces, which are formed by the three sets of planes of the
643 $\{112\}$, $\{121\}$, and $\{211\}$ families, as shown in insertion at
644 Fig. 6d.

645 FE-SEM images showed in Fig. 6e–h for $\beta\text{-Ag}_2\text{MoO}_4$
646 microcrystals synthesized by the SC method exhibit the
647 presence of a large quantity of potatoes-like with somewhat
648 porous surfaces. However, these $\beta\text{-Ag}_2\text{MoO}_4$ microcrystals
649 have a shape with average crystal sizes ranging from 3.65
650 to 7.58 μm and an average crystal size of approximately
651 5.6 mm. crystal growth is indirectly by direct interaction
652 the ultrasonic wave with the H_2O molecules. In this case, we
653 have the heterogeneous sonochemical process of liquid–solid
654 systems in constant contact, as reported in the literature [29,
655 34].

The $\beta\text{-Ag}_2\text{MoO}_4$ microcrystals synthesized by the HSI-
IFC method present several pores and roughness on the sur-
face of large irregular crystals, as shown by FE-SEM images
in Figs. 6k, l. This behavior is due to the fast ions injection
method, which enables high superheating localized in the
aqueous solution and accelerates the growth of large solid
particles faster [70]. In this way, these large $\beta\text{-Ag}_2\text{MoO}_4$
microcrystals have a shape with average crystal sizes rang-
ing from 4.85 to 20.9 μm and an average crystal size of
approximately 12.88 mm.

Finally, the FE-SEM images shown in Figs. 6m–p the
presence of $\beta\text{-Ag}_2\text{MoO}_4$ microcrystals obtained by the CH
synthesis method with non-homogeneous shapes, irregular
polyhedrons related to concave trisoctahedra with different
facets, and also rhombic dodecahedrons ascribed as irregular
polyhedrons. These $\beta\text{-Ag}_2\text{MoO}_4$ microcrystals have shapes
with sizes ranging from 3.31 to 7.35 μm and an average
crystal size of approximately 5.36 mm. These crystals at
the final growth state of CH synthesis present an increase in
facets numbers and forms the rhombic dodecahedron-like
 $\beta\text{-Ag}_2\text{MoO}_4$ microcrystals, which are formed by the three
sets of planes of the $\{110\}$, $\{011\}$, and $\{101\}$ families,
which exhibits twelve faces lozenge-like, as shown in inser-
tion at Fig. 6p. In addition, the CH synthesis method allows
the formation of some rhombic dodecahedron shapes still
in the process of maturation and definition of their facets
for smoother surfaces. It is also seen in the formation of sil-
ver nanoparticles (NPsAg) on the surface of these crystals,
Fig. 6p, which are associated with photosensitivity of Ag
against the electron beam used in the analysis of FE-SEM
image [71].

These $\beta\text{-Ag}_2\text{MoO}_4$ microcrystals with rhombic dodeca-
hedron shapes are associated with the oriented aggregation
mechanism, which involves the spontaneous self-organiza-
tion of adjacent particles along a common crystallographic
orientation. Table 4a–c show the data employed to model
 $\beta\text{-Ag}_2\text{MoO}_4$ crystals shapes (CP and CH method) using the
KrystalShaper Crystal Morphology Editor/Viewer software
Version 1.5.0 [72] using our lattice parameter values, dis-
tances, and Miller indices (h, k, l) from Rietveld refinement
data.

These sets of planes presented in Table 4a–c allow an
understanding of the growth processes, appearance, or
disappearance of a certain plane due to changes in surface
energies of microcrystals obtained using the CP and CH
synthesis methods.

3.7 UV–Vis Spectroscopy Analyses

It was possible to obtain information about the region of
maximum absorption in the electromagnetic spectrum, band-
gap energy, degree of order–disorder, and intermediate lev-
els between the valence band (VB) and conduction band

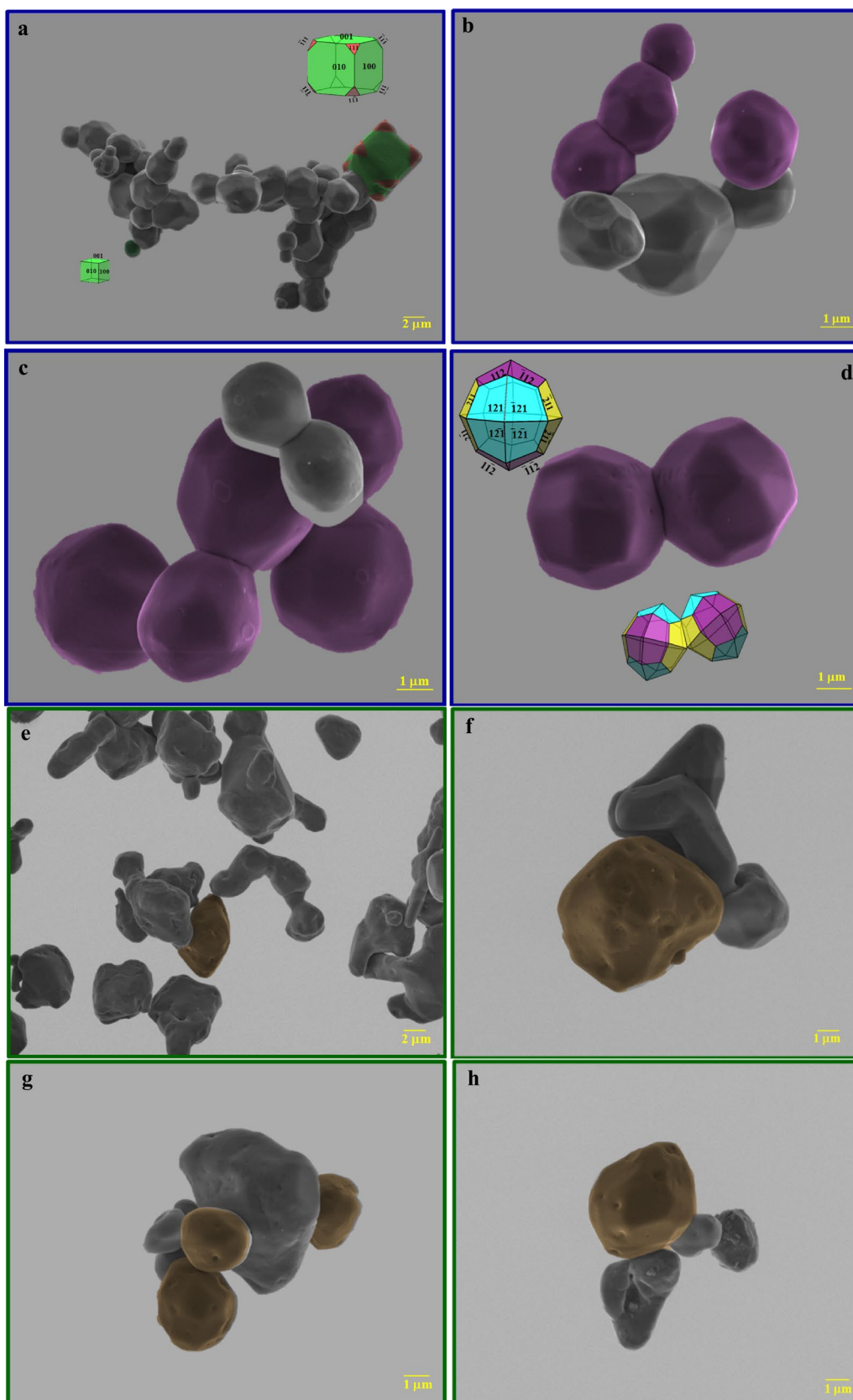


Fig. 6 a–p: FE-SEM images of β - Ag_2MoO_4 microcrystals made by the a–d CP, e–h SC, k, l HSIIFC, and m–p CH synthesis methods

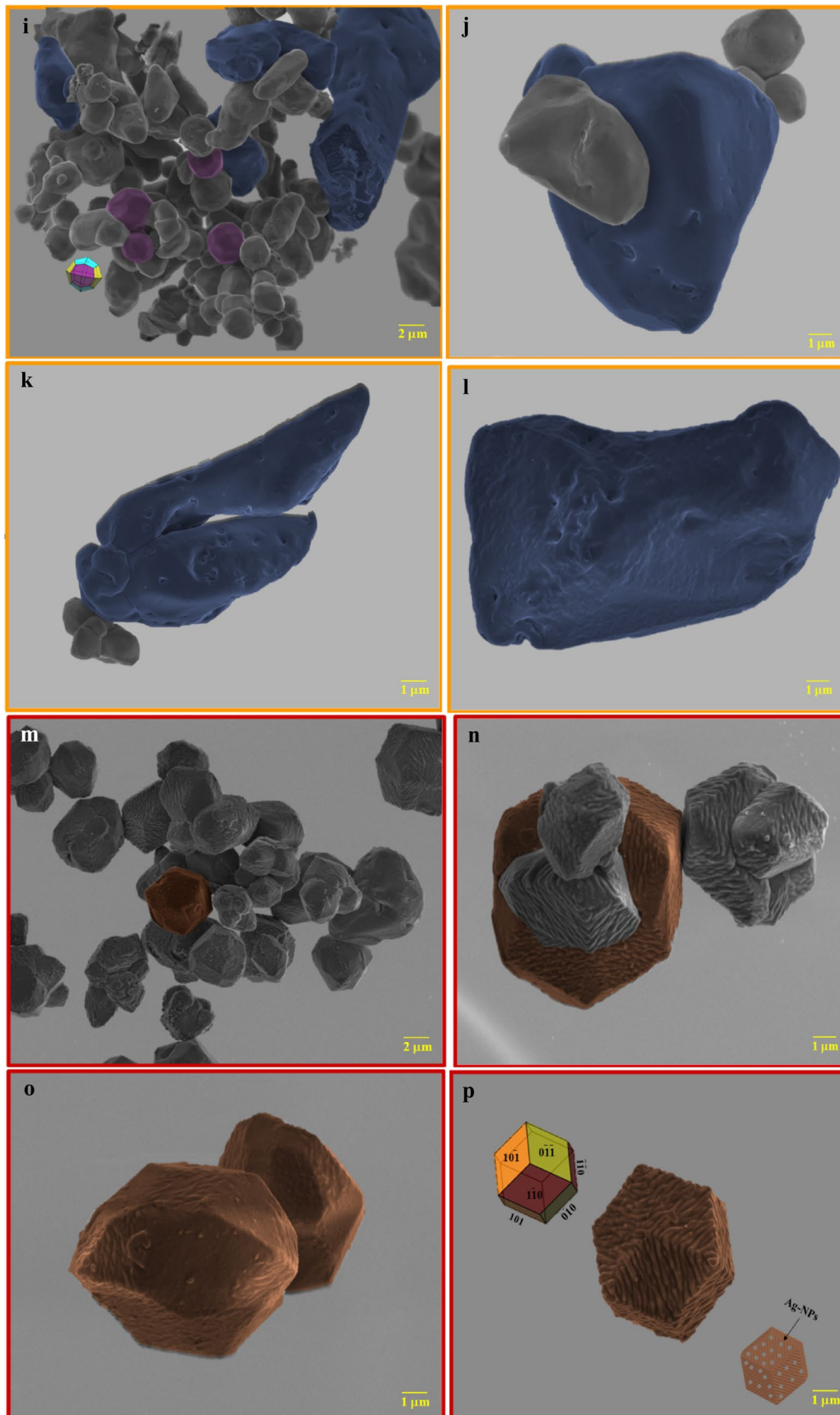


Fig. 6 (continued)

(CB) of $\beta\text{-Ag}_2\text{MoO}_4$ microcrystals prepared by different methodologies. For example, the value of the forbidden E_{gap} was calculated by the methodology proposed by Kubelka and Munk [73] that relates the absorbance, the photon, and the type of electronic transition of the material, used in limited cases of very thick samples [74]. Such as equation is based on the diffuse reflectance transformation to estimate the E_{gap} values with perfection, as seen in Eq. (7):

$$F(R_{\infty}) = \frac{(1 - R_{\infty})^2}{2R_{\infty}} = \frac{k}{s} \quad (7)$$

where: $F(R_{\infty})$ is the Kubelka–Munk function or total sample reflectance; K is the apparent molar absorption coefficient, and; S is the apparent scattering coefficient.

For this work, barium sulfate (BaSO_4) was used as a “blank” background or standard sample in the reflectance analyses, $R_{\infty} = R_{\text{sample}}/R_{\text{BaSO}_4}$. In a parabolic band structure (in the case of prepared $\beta\text{-Ag}_2\text{MoO}_4$ microcrystals), can be determined the E_{gap} and the absorption coefficient of semiconductor oxides [74, 76] through Eq. (8):

$$\alpha h\nu = C_1(h\nu - E_{\text{gap}})^n \quad (8)$$

where α is the linear absorption coefficient of the material, $h\nu$ is the photon energy, C_1 is a proportionality constant, E_{gap} is the bandgap energy or optical gap, and n is a constant related to different types of electronic transitions in semiconductors. The $n=0.5$ is related to materials with E_{gap} permitted direct, $n=2$ for permitted indirect, $n=1.5$ for prohibited direct, and $n=3$ for prohibited indirect transitions.

According to theoretical studies reported in the literature, $\beta\text{-Ag}_2\text{MoO}_4$ microcrystals present an optical absorption spectrum conducted by indirect transitions [36, 64]; that is, when the electronic absorption process occurs, the electrons that are in minimum energy states in the conduction band (CB), manage to return to the maximum states, in the valence band (VB) at different points in the Brillouin zone [64].

Therefore, $n=2$ was used in Eq. (8) to calculate the E_{gap} for the $\beta\text{-Ag}_2\text{MoO}_4$ microcrystals prepared using the CP, SC, HSIIFC, and CH methods. Then, applying $K=2\alpha$ to the absolute reflectance function, the Kubelka–Munk function is simplified according to Eq. (9):

$$F(R_{\infty})h\nu^{0.5} = C_2(h\nu - E_{\text{gap}})^n \quad (9)$$

Thus, drawing a graph with the values of $[F(R_{\infty})h\nu]^{0.5}$ (y-axis) determined by Eq. (9) as a function of the photon energy (eV) at (x-axis) and performing a linear extrapolation on the part straight line of the spectra (extrapolation of the linear fit) of UV–Vis, allowed to obtain the E_{gap} values for the prepared materials, seen in Figs. 7c–f. Furthermore, the maximum absorption of $\beta\text{-Ag}_2\text{MoO}_4$ microcrystals is

described from the graphic relationship of wavelength values (λ) at (x-axis) with absorbance values at (y-axis), Fig. 7a–b.

Figure 7a displays the maximum absorption spectra of the synthesized $\beta\text{-Ag}_2\text{MoO}_4$ microcrystals in the region comprising ultraviolet radiation, and there are three main absorptions located at approximately 280, 310, and 340 nm. This result indicates that it is necessary to use lamps with a wavelength in this region to generate electron/hole pairs (e^-/h^+) in the photocatalytic process [77, 78]. In case related to UV-C ($\lambda_{\text{max}} = 254 \text{ nm} \approx 4.88 \text{ eV}$), UV-B ($\lambda_{\text{max}} = 306 \text{ nm} \approx 4.05 \text{ eV}$), UV-A ($\lambda_{\text{max}} = 365 \text{ nm} \approx 3.40 \text{ eV}$) and visible ($\lambda_{\text{max}} = 541 \text{ nm} \approx 2.29 \text{ eV}$) [79]. Magnification of the highlighted section of the UV–Vis absorption spectra, Fig. 7b, showed that $\beta\text{-Ag}_2\text{MoO}_4$ microcrystals made by the CH method have a pronounced absorption band in the visible region. This fact may be associated with its low structural order (confirmed in XRD, Rietveld Refinement, and micro-Raman analyses), caused by crystalline defects generated by pressures and temperature during hydrothermal treatment [31]. Figures 7c–f show that using these experimental methods makes it possible to obtain UV–Vis spectra with an indirect electronic transition profile, with optical behavior characteristic of structurally ordered crystalline materials, as demonstrated in XRD analyses. The E_{gap} values for the microcrystals prepared by the CP, SC, HSIIFC, and CH synthesis methods were as follows: 3.3; 3.27; 3.26, and 3.25 eV, respectively. These E_{gap} values agree with the experimental results already reported for this material, evidencing the reliability of the methodologies used in this article.

It is also possible to observe that these different synthesis techniques provide changes in the E_{gap} values, which may be associated with variations in terms of external forces, such as temperature and pressure, which act directly on the ordering of the structure, promoting the emergence of levels of intermediate energies between the VB of CB, which are associated with the degree of structural disorder of the undistorted tetrahedral [MoO_4] and distorted octahedral [AgO_6] clusters. According to the literature, more ordered structures, such as $\beta\text{-Ag}_2\text{MoO}_4$ microcrystals made by the CP method, have few intermediate energy levels between the VB and CB. Consequently, a higher E_{gap} , on the other hand, are materials that have defects in their crystal lattice, as well as the microcrystals obtained via the HC method, which have the lowest structural order, and, therefore, the lowest E_{gap} value among other materials [31].

3.8 Colorimetric Data Analysis

To quantify the colorimetric coordinates of $\beta\text{-Ag}_2\text{MoO}_4$ microcrystals made by CP, SC, HSIIFC, and CH synthesis methods, the CIELAB color space, established by the International Commission on Illumination (CIE) in 1976 [47]

Table 4 (a–c) Average lattice parameters, angles, Laue Group ($m\bar{3}m$), Miller indices (h, k, l) to the notation of lattice planes and dis-tances used in the computational modeling with different crystallographic planes of β - Ag_2MoO_4 microcrystals synthesized by the (a,b) CP, and (c) CH synthesis methodsa) β - Ag_2MoO_4 -CP method

Lattice parameter $a=b=c=9.257781$ (Å) and number of faces of cube-like β - Ag_2MoO_4 crystal	Miller index (hkl)	Distance	Lattice parameter $a=b=c=9.257781$ (Å) and number of faces of cuboctahedron-like β - Ag_2MoO_4 crystal	Miller index (hkl)	Distance
1°	1 0 0	0.5	1°	1 0 0	0.5
2°	0 1 0	0.5	2°	0 1 0	0.5
3°	0 -1 0	0.5	3°	0 -1 0	0.5
4°	-1 0 0	0.5	4°	-1 0 0	0.5
5°	0 0 -1	0.5	5°	0 0 -1	0.5
6°	0 0 1	0.5	6°	0 0 1	0.5
–	– – –	–	7°	1 1 1	0.75
–	– – –	–	8°	1 1 -1	0.75
–	– – –	–	9°	1 -1 1	0.75
–	– – –	–	10°	-1 -1 1	0.75
–	– – –	–	11°	-1 1 1	0.75
–	– – –	–	12°	1 -1 -1	0.75
–	– – –	–	13°	-1 -1 -1	0.75
–	– – –	–	14°	-1 1 -1	0.75

b) β - Ag_2MoO_4 -CP method

Lattice parameter $a=b=c=9.257781$ (Å) and number of faces of trapezohedron-like β - Ag_2MoO_4 crystal	Miller index (hkl)	Distance
1°	2 1 1	1.0
2°	1 2 -1	1.0
3°	1 -2 1	1.0
4°	-2 -1 1	1.0
5°	-1 2 1	1.0
6°	2 -1 -1	1.0
7°	-1 -2 -1	1.0
8°	-2 1 -1	1.0
9°	-1 -1 -2	1.0
10°	1 2 1	1.0
11°	-2 -1 -1	1.0
12°	1 1 2	1.0
13°	1 -1 2	1.0
14°	1 -2 -1	1.0
15°	2 1 -1	1.0
16°	-1 1 -2	1.0
17°	1 1 -2	1.0
18°	-1 2 -1	1.0
19°	-2 1 1	1.0
20°	-1 -1 2	1.0
21°	-1 1 2	1.0
22°	-1 -2 1	1.0
23°	2 -1 1	1.0
24°	1 -1 -2	1.0

Table 4 (continued)c) β -Ag₂MoO₄-CH method

Lattice parameter $a=b=c=9.317389$ (Å) and number of faces of rhombic dodecahedron-like β -Ag ₂ MoO ₄ crystal	Miller index (hkl)			Distance
1°	1	1	0	1.0
2°	1	-1	0	1.0
3°	-1	-1	0	1.0
4°	-1	1	0	1.0
5°	-1	0	-1	1.0
6°	0	1	1	1.0
7°	1	0	-1	1.0
8°	0	1	-1	1.0
9°	1	0	1	1.0
10°	0	-1	-1	1.0
11°	-1	0	1	1.0
12°	0	-1	1	1.0

was used. The colorimetric analyses were performed in three average readings of 90° angles for each synthesized material. The CIELAB system is the most used and recognized color space worldwide. Its standard or “white” has been widely used as a reference to measure the colors of materials, particularly in colorimetric equipment, as well as the colorimeter [80, 81]. The main contribution of the CIELAB color space, since its creation in 1976, was to reduce Yxy space divergences (equal distances on the xy chromaticity diagram, which do not correspond to equal perceived color differences). L* represents lightness in this color space, and a* and b* are chromaticity coordinates. The colorimetric coordinates a* correspond to (-a = green) and (+a = red) in the x-axis values, and the colorimetric coordinates b* correspond to (-b = blue) and (+b = yellow) in the values on the y-axis, L* is related to luminosity, and its value on the z-axis can vary (from 0 = black to 100 = white) [81–84].

The results of the combinations of different colors for the β -AgMoO₄ criteria, obtained by different synthesis routes, presented different values of L*, a*, and b*. These results are presented in Table 5. Other results are presented through 2D circles, using β -AgMoO₄ scales like all β -AgMoO₄ nuclei shown in Figs. 8a–d.

The β -AgMoO₄ microcrystals made by the HSIIFC method showed the highest values of L* and a*, followed by those prepared via the CP and SC routes, indicating that these methods allow the crystallization of β -AgMoO₄ crystals with different colors, according to the colorimetric coordinates (L*, a*, b*). The hexadecimal color code found according to the colorimetric coordinates for the β -AgMoO₄ microcrystals made by the HSIIFC method was #8c8373. This code is related to a shade of brown (Fig. 8a) which in the RGB color model is composed of 54.9% red, 51.37% green, and 45.1% blue. This color has an approximate

wavelength of 577.1 nm. The closest name to this color is Zinc Luster, shown in Table 5. On the other hand, those obtained by the CP method presented the following hexadecimal color code #8c8274, associated with a light brown tone (Fig. 8b). This hexadecimal code for the RGB color model consists of 54.9% red, 50.98% green, and 45.49% blue and has an approximate wavelength of 578.45 nm. The closest name for this color is Nile Clay, described in Table 5. However, the SC method obtained microcrystals with a brown medium with the following hexadecimal color code #847d71 (Fig. 8c). According to the RGB color model, #847d71 is composed of 51.76% red, 49.02% green and 44.31% blue (Fig. 8c). This color has an approximate wavelength of 577.16 nm. The most equivalent name for this color is Gray (Crayola), given in Table 5.

On the other hand, the β -AgMoO₄ microcrystals made by the CH route showed lower L* and a* values, indicating that these samples are darker; the materials obtained by this method crystallize in a dark brown color, with the following hexadecimal color code #59554d, which in the RGB color model is composed of 34.9% red, 33.33% green and 30.2% blue ((Fig. 8a). This color has a wavelength of 576.31 nm. The name found for this color was Charcoal Brown. These differences in the coordinates of color changes (L* a*, and b*) can be methods at a time of synthesis of optical properties (crystal size values) morphological (methods and sizes of optical properties) can be methods at a time of synthesis and sizes of optical properties [42, 43] as well as already, previous sessions. According to the digital photos, such changes were altered as changes in pigmentation between the materials obtained, for shades of light brown to dark brown, which are available in Table 5. Notably, the changes in microcrystal pigmentation were perfectly correlated with all qualitative color parameters (L*, a*, b*)

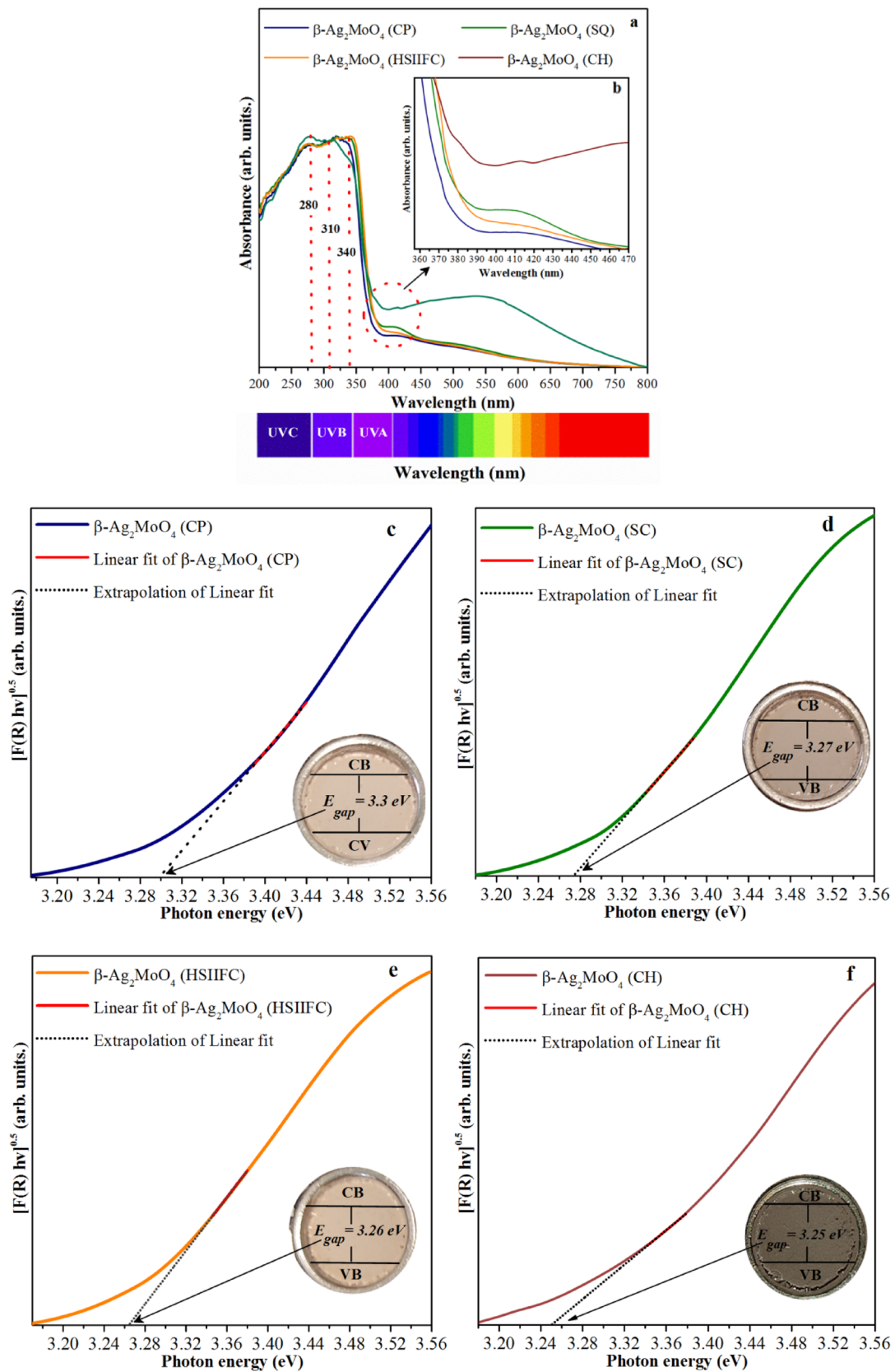


Fig. 7 a–f UV–Vis absorption spectrum (a), highlighted section magnification (b), and diffuse reflectance mode UV–Vis spectra for $\beta\text{-Ag}_2\text{MoO}_4$ microcrystals prepared by the (c) PC, (d) HSIIFC (d), e SC, and f CH synthesis methods

875 acquired in the FRU® color software version 3.22 and with
876 the visual qualitative parameters obtained by high-quality
877 digital photos. Captured quality of β -AgMoO₄ microcrystals
878 (closest observed color) used to record the RGB and
879 HEX values, shown in Table 5, using the Color Detector
880 software—Instant Color Detect, version 1.0.1.

881 From the values of colorimetric coordinates (L^* , a^* , and
882 b^*) of the β -Ag₂MoO₄ microcrystals obtained by the CP,
883 SC, HSIIFC, and CH synthesis methods, it is also possible
884 to determine the energy difference (ΔE), the chromaticity
885 (C) and the hue angle (H°), using Eqs. (10–12).

$$886 \Delta E = \sqrt{(\Delta L^*)^2 + (\Delta a^*)^2 + (\Delta b^*)^2} \quad (10)$$

$$888 C = \sqrt{(a^*)^2 + (b^*)^2} \quad (11)$$

$$890 H = \tan^{-1}\left(\frac{b^*}{a^*}\right) \quad (12)$$

891 where ΔE is the energy difference between the colored
892 media, ΔL represents the difference in brightness between
893 two live surfaces, and Δa^* and Δb^* are the differences in
894 the color coordinates a^* and b^* , respectively. C is related to
895 the vividness or opacity of a color, how close the color is to
896 gray, or the pure matrix. Finally, H is related to one of the
897 main properties, called color appearance parameters, and
898 describes how similar or a different color is to the stimuli
899 described by red (**R**), green (**G**), blue (**B**), or yellow (**Y**).

900 The β -AgMoO₄ microcrystals obtained by the HSIIFC
901 method show a higher C , H , and ΔE (shown in Table 5)
902 than the microcrystals synthesized by the other methods.
903 This fact can be attributed to its E_{gap} value, particle size,
904 and irregular shape. On the other hand, the microcrystals
905 synthesized by CP showed lower opacity and greater energy
906 difference among the other prepared materials, which can
907 also be attributed to the particles' size, shape, and E_{gap} value.

908 Therefore, it can confirm through the colorimetric analy-
909 sis that using these different preparation methodologies pro-
910 motes the crystallization of β -AgMoO₄ microcrystals with
911 different colors and values of colorimetric coordinates close
912 or distant from each other. It is also worth remembering that
913 there are no brief or detailed studies regarding the colorim-
914 etric properties of this material so far. This article is the
915 pioneer in the quantification of colorimetric coordinates and
916 description of the closest color name of β -AgMoO₄ micro-
917 crystals made by different methods.
918

919 3.9 Theoretical Analysis of Surface Energies 920 for β -AgMoO₄ Crystals

921 The experimental results reveal that the method of syn-
922 thesis caused a morphological change in the β -AgMoO₄

microcrystals. In order to analysis these morphologies at
structural level, the surfaces models of the exposed surfaces
presented in all crystals shape were constructed and these
models and the results of the first-principles calculation are
shown in Figs. 9a–d. All surfaces present oxygen vacancies
(V_{O}) in the last layer, resulting in uncoordinated Ag and
Mo clusters. The $[\text{AgO}_5\text{-}V_{\text{O}}]$ clusters are present only in the
(001) surface, while the $[\text{AgO}_4\text{-}2V_{\text{O}}]$ clusters are present in
the (011) and (112) surfaces. In the (111) and (112) surfaces
exist the $[\text{AgO}_3\text{-}3V_{\text{O}}]$ clusters and in the last one, also exist
the $[\text{AgO}_5\text{-}1V_{\text{O}}]$ clusters.

As we can see, the (112) surface, in which present a
high-index of Miller, is more stable than the (001) and
(011) surfaces, resulting in the follow order of stability:
(111) > (112) > (011) > (001) with E_{surf} values of 0.77,
1.06, 1.29, and 1.91 J/m², respectively. From these E_{surf}
values associated to the Wulff construction the equilibrium
morphology (ideal) was achieved theoretically, in which
is mainly formed by the (111) surface, as illustrated in the
Fig. 9e.

From this equilibrium morphology, we also modulated
the experimental morphologies (namely as 3) where the 3a
and 3c morphologies were obtained by the CP method, while
the 3b was obtained by the CH method. These morphologies
were achieved by passing through two intermediate mor-
phologies (namely as 1 and 2). To obtain the reaction path
that interconnect the ideal, the intermediates and the experi-
mental morphologies, we also calculated their E_{pol} values.
This value represented the surface energy of the polyhedrons
by the crystal area. As we can see in Fig. 9e, the morphol-
ogy obtained by the CP method (3c) presented the highest
 E_{pol} value and its formed by only the surfaces with (112)
plane. Although, the (112) surface present a low E_{surf} value
in which means that surface is stable, the E_{pol} value suggest
that this crystal shape should be more reactive for having
more energy by area.

923 3.10 Photocatalytic Assays Analysis

924 The evaluation of the photocatalytic property of the synthe-
925 sized samples was verified in the degradation of the RhB dye
926 solution under irradiation of different lamps with absorption
927 in the UV region, namely UV-C, UV-A, UV-B, and visible.
928 These results are shown in Figs. 10a–e.

929 Figures 10a–e show the study of the relative decay of
930 RhB dye solution concentration (C_{n}/C_0) vs. exposure time to
931 UV and visible light. The first 30 min in the dark only rep-
932 represents the adsorption/desorption equilibrium of the target
933 compound. After this process, the RhB dye solution showed
934 a reduction in its concentration, indicating the existence of
935 photocatalytic degradation in all systems. The efficiency in
936 the degradation rate, shown in Fig. 10e, was carried out to
937 verify the influence of these different synthesis methods on
938

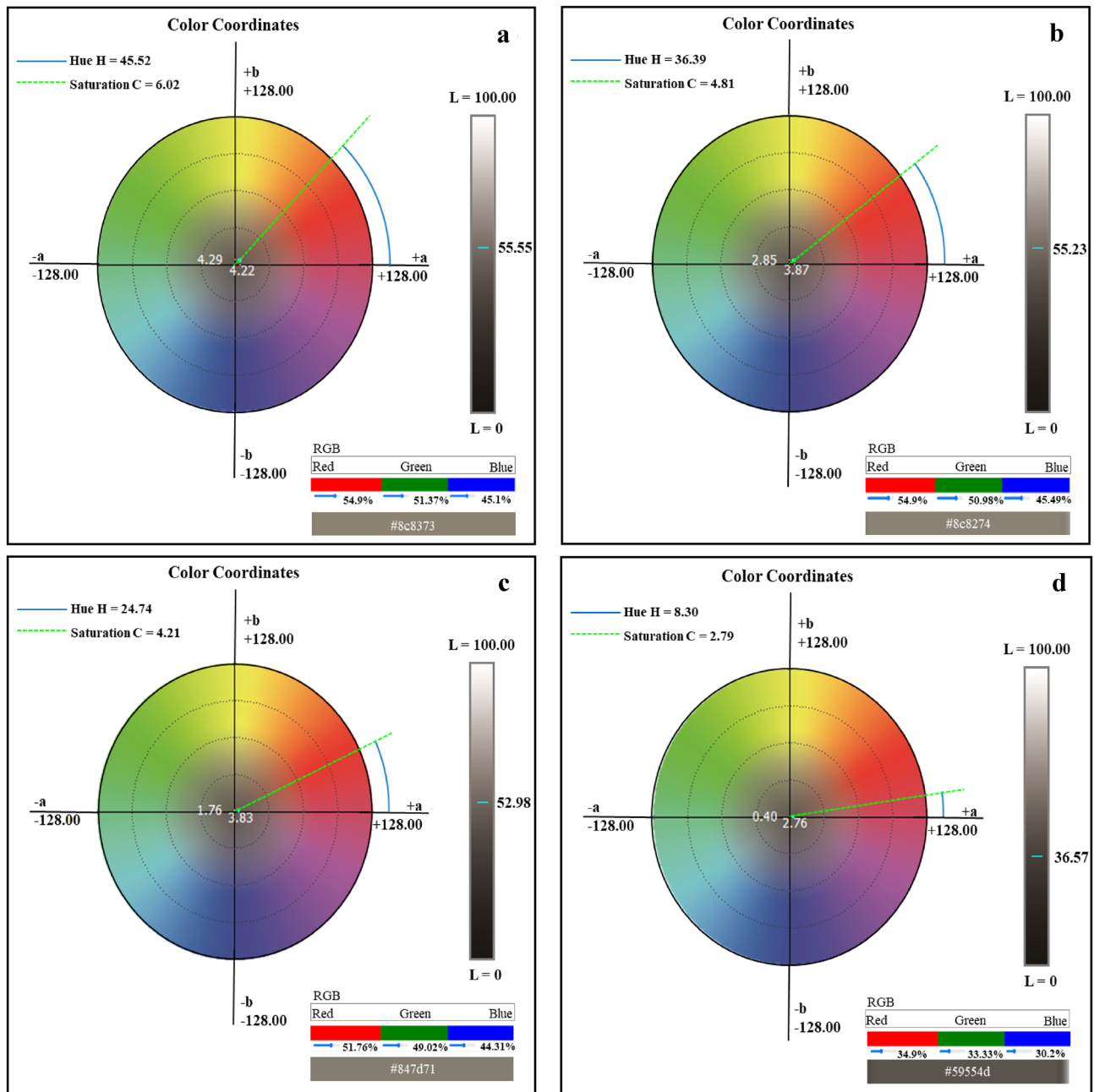









Fig. 8 a–d: 2D color circle with L*, a*, and b* chromaticity diagram according to CIELAB (1976) color space and RGB values for β - Ag_2MoO_4 microcrystals synthesized by the **a** HFIISC, **b** CP **c** SC, and **d** CH synthesis methods

974 the photocatalytic property of pure β - Ag_2MoO_4 microcrystals, as well as their behavior under different types of irradiations. For the photolysis process, in which the target compound was subjected only to irradiation for 240 min, UV-C, UV-A, UV-B, and visible light, the degradation rates were 5; 1.72; 2.2, and 1.8%, respectively. In this case, the degradation of the RhB dye solution occurs through the absorption of photons by photolysis [85]. These degradation rate values demonstrate that this exposure to different UV and visible

983 light alone cannot significantly affect the concentration of this pollutant, thus confirming its high resistance to this type of irradiation [86] and the need for a photocatalyst such as β - Ag_2MoO_4 microcrystals [30].

984
985
986
987 On the other hand, the target compound was subjected to the photocatalysis process described in Figs. 10a–d, in which the irradiation of different lamps was used, in addition to the use of β - Ag_2MoO_4 microcrystals, made by the CP, SC, HSI-IFC, and CH methods as a catalyst, there was a significant

Table 5 Colorimetric coordinates and color names for β - Ag_2MoO_4 microcrystals synthesized by HSIIFC, CP, SC, and CH synthesis methods

SM	L*	a*	b*	ΔE^*	C*	H*	* RGB Measured	*HEX Measured	*Nearest Color found	**Nearest Color Observed	**RGB Observed	**HEX Observed
β - Ag_2MoO_4 HSIIFC	55.55	4215	4,2925	55,8748	6,01,596	45,5222	140, 131, 115	#8c8373	 <i>ter</i>		209,185, 162	#d1b9a2
β - Ag_2MoO_4 CP	55.227	387	2,8525	55,4363	4,8076	36,3931	138, 130, 116	#8c8274	 <i>y</i>		217,197, 177	#d9c5b1
β - Ag_2MoO_4 SC	52.976	3,8266	1,7633	53,1439	4,21,339	24,7402	132, 125, 113	#847d71	 <i>er</i>		181,162, 147	#b5a293
β - Ag_2MoO_4 CH	36.566	2,7633	-0,4033	36,6731	2,7926	8,3064	89, 85, 77	#59554d	 <i>ayola</i> <i>l Brown</i>	 <i>enue</i>	102, 90, 74	#665a4a

RGB is the abbreviation of an additive colour system in which R is red, G is the green, and B is the blue, HEX = is the abbreviation for the hexadecimal notation of the colours,

SM Synthesis method; HSIIFC Hot Solution Ion Injection with Fast Cooling; PC Controlled Precipitation; SC Sonochemical; CH Conventional Hydrothermal; L Luminosity, ΔE energy difference between samples; C Chroma; and H the hue angle

a*(+a* indicates the red colour and -a* indicates the green colour)

b*(+b* indicates the yellow colour and -b* indicates the blue color)

*Obtained with Color Software FRU@ version 3.22 and ** Color detector—instant colour detect version 1.1

improvement in the rate values of discoloration compared to photolysis. This improvement is related to the appearance of highly reactive species (such as H^{\cdot} , HO^{\cdot} , HO_2^{\cdot} , and $O_2^{\cdot-}$) that are responsible for the mineralization of molecules in the RhB solution. These reactive species are generated through oxidation reactions (in VB) and reduction (in CB), caused by the interaction of the e^-/h^+ pair with electron acceptors/donors (e^-) (most commonly H_2O , O_2 , and $OH^{\cdot-}$) dissolved during the photocatalysis process [87, 88]

These reactions are initiated due to the activation of $\beta\text{-Ag}_2\text{MoO}_4$ microcrystals, caused by the irradiation of different UV and visible light, which stops this material was sufficient to promote the excitation of e^- from BV (by presenting an $E > E_{\text{gap}}$ value of the synthesizing materials) to CB, generating a gap or hole (h^+) in VB. This mechanism is known as e^-/h^+ pair formation. In addition, these pairs can recombine, releasing energy in the form of heat and contributing to the degradation of the pollutant.

The analysis of Fig. 10e also allows us to observe a decrease in the degradation efficiency as the tests were carried out in the different light systems. There was no synergism between catalysts and the change in irradiation type. The best photocatalysis results in the discoloration rate of the RhB solution were obtained in the catalytic system with UV-C lamps. Among the catalysts tested in this radiation, those prepared by the CP method showed the most promising results, getting a discoloration rate of 85.12%, followed by the microcrystals made by the HSIIFC methods (72.09%), CH (52.53%), and SC (39%). UV-C light presents more energetic beams, which increases the yield of the percentage of excited electrons, and, consequently, the efficiency of the photocatalytic process. This type of radiation also has a higher ionization potential, which facilitates the interaction of the RhB dye molecules with the catalyst more strongly, favoring the breaking of their chemical bonds [89, 90]. The better photocatalytic efficiency of $\beta\text{-Ag}_2\text{MoO}_4$ microcrystals prepared by the PC method may be associated with their higher crystallinity, evidenced in the structural analysis of XRD, Micro Ramam, and FTIR, as well as its trapezoidal morphology that provides more reaction sites in the photocatalytic degradation process [90], due to the greater number of faces that are available to react in the catalytic medium (24 trapezoidal faces), the more significant number of facets available to control react in the catalytic medium and E_{gap} values, are close to the energy (3.3 eV) of UV-C light. These factors, associated with the high energy of UV-C light, contributed to a more excellent formation of free radicals responsible for the mineralization of the target compound. Thus, its structural, morphological, and optical organization proved to be ideally favorable (among the conditions investigated in this work) to achieve the highest performance in the degradation of the RhB dye solution under 240 min irradiation at different wavelengths of UV and visible light.

Good results were also observed in the degradation rate of the RhB dye solution when using $\beta\text{-Ag}_2\text{MoO}_4$ microcrystals made via the IISQRR route (72.09%). He attributes this result to the presence of trapezoidal particles, as obtained in the CP method (Fig. 6d), which join the irregular particles (Fig. 6i). It is clear that this type of morphology effectively contributes to the photocatalytic activity of $\beta\text{-Ag}_2\text{MoO}_4$.

The least significant results of photocatalysis were detected for the catalysts made by the SC method, in which the degradation rate in almost all systems was the lowest. This fact may be associated with a high rate of electronic recombination, low stability, and its (potato) morphology, which provides insufficient active sites for the catalytic process [34]. In the visible light system, the best results of the degradation rate of the RhB dye solution were seen for the catalysts made by the CH method. A possible explanation for this may be the lower E_{gap} value, caused by structural defects already discussed in the previous sections, which allowed the $\beta\text{-Ag}_2\text{MoO}_4$ (CH) microcrystals to present an E_{gap} value closer to the energy of Vis-light. We can also relate to the appearance of the pronounced absorption band in the visible region, as previously seen in Fig. 7a, b, and the appearance of Ag^0 on the surface of these crystals, induced by visible light radiation. This phenomenon is due to the fact that Ag presents photosensitivity and, therefore, can be easily reduced [71], being more characteristic in this study for materials obtained by the HC method, as evidenced in the FE-SEM images the Fig. 6p.

4 Conclusions

In summary, it was possible to prepare with success pristine $\beta\text{-Ag}_2\text{MoO}_4$ microcrystals by the CP, SC, HSIIFC, and CH synthetic methods and to evaluate the effect of these methodologies on their structural, morphological, optical, colorimetric, and photocatalytic properties. The structural characterizations of XRD, Rietveld refinement, and micro-Raman and FTIR spectroscopies confirmed that the $\beta\text{-Ag}_2\text{MoO}_4$ microcrystals prepared by these different methodologies exhibit a cubic spinel-like structure with lattice parameters ($a = b = c = 9.6 \text{ \AA}$), space group ($Fd\bar{3}m$), point group symmetry (O_h^h) and eight molecular formulas per unit cell ($Z = 8$). These results reported in this paper are very good and in agreement with those described in the ICSD database, card N° 36,187. Also observed are that these methods make it possible to obtain microcrystals with a long-range crystallinity goal. The $\beta\text{-Ag}_2\text{MoO}_4$ microcrystals made by the CH method exhibited the highest unit cell volume value (808.877 \AA^3), followed by those prepared by the other methods (794.046 \AA^3 for SC, (793.4521 \AA^3) for CP, and (787.635 \AA^3) for HSIIFC. On the other hand, the relative positions of the O atoms showed

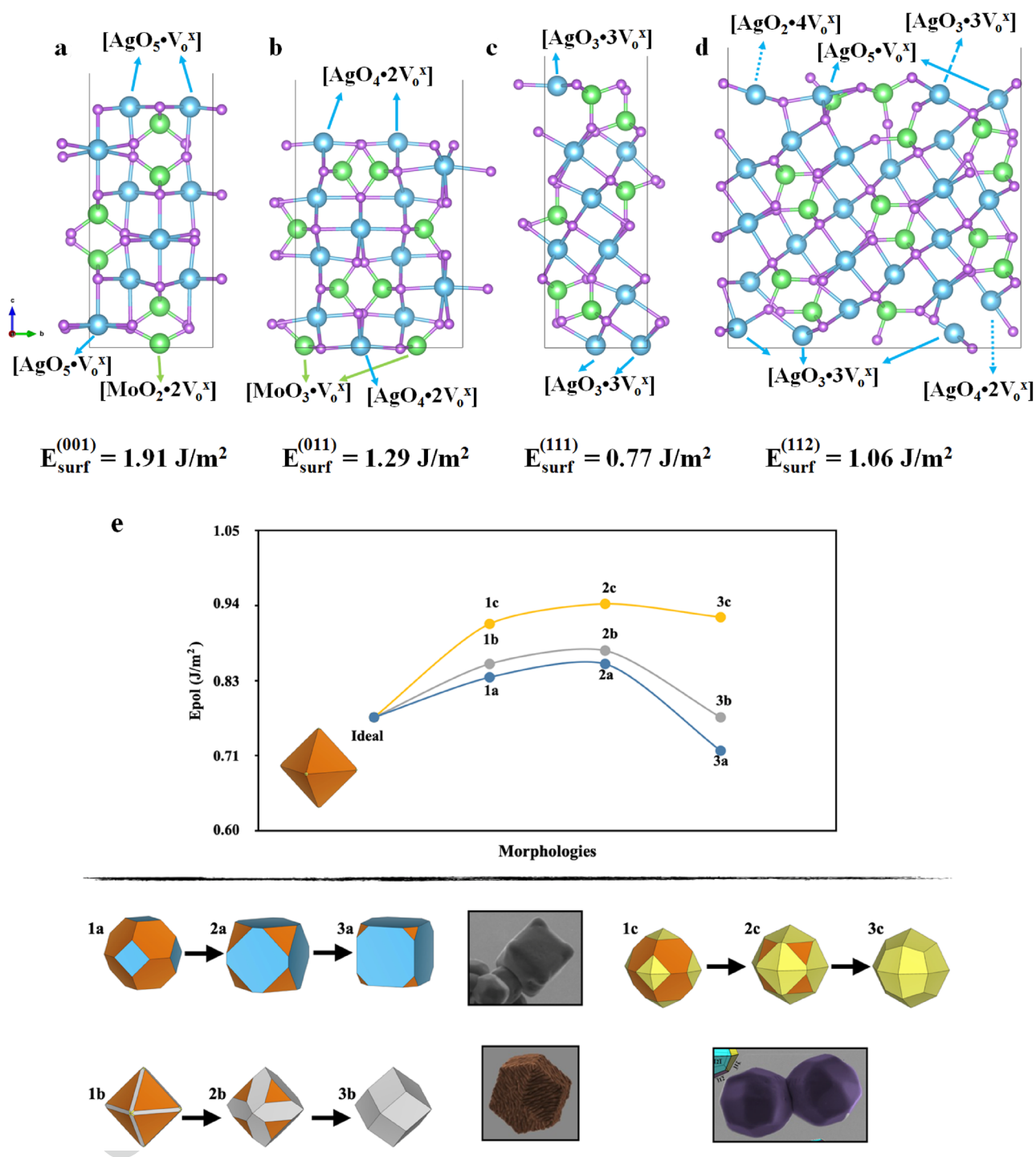


Fig. 9 a–e: Surface models with their undercoordinated clusters and E_{surf} values for: **a** 001, **b** (011), **c** (111), and **d** (112). **e** Evolution of the crystal shape observed experimentally from the equilibrium morphology (ideal). 1a, 1b, 1c and 2a, 2b, 2c morphologies are interme-

diated, while the experimental morphologies are represented by 3a, 3b and 3c. The surface colors are given as: (001) in blue, (011) in gray, (111) in orange, and (112) in yellow

1095 minor variations, while the Ag and Mo atoms remained
 1096 fixed in their positions in the structure. From the construction
 1097 of the microcrystal's unit cells, it is possible to visualize
 1098 the presence of two types of clusters, one formed by

1099 distorted octahedral $[\text{AgO}_6]$ clusters, with two different
 1100 bond angles between the Ag and O atom (O–Ag–O) and
 1101 other undistorted tetrahedral $[\text{MoO}_4]$ clusters, with equal
 1102 bond angles (O–Mo–O). FE-SEM images shown that it is

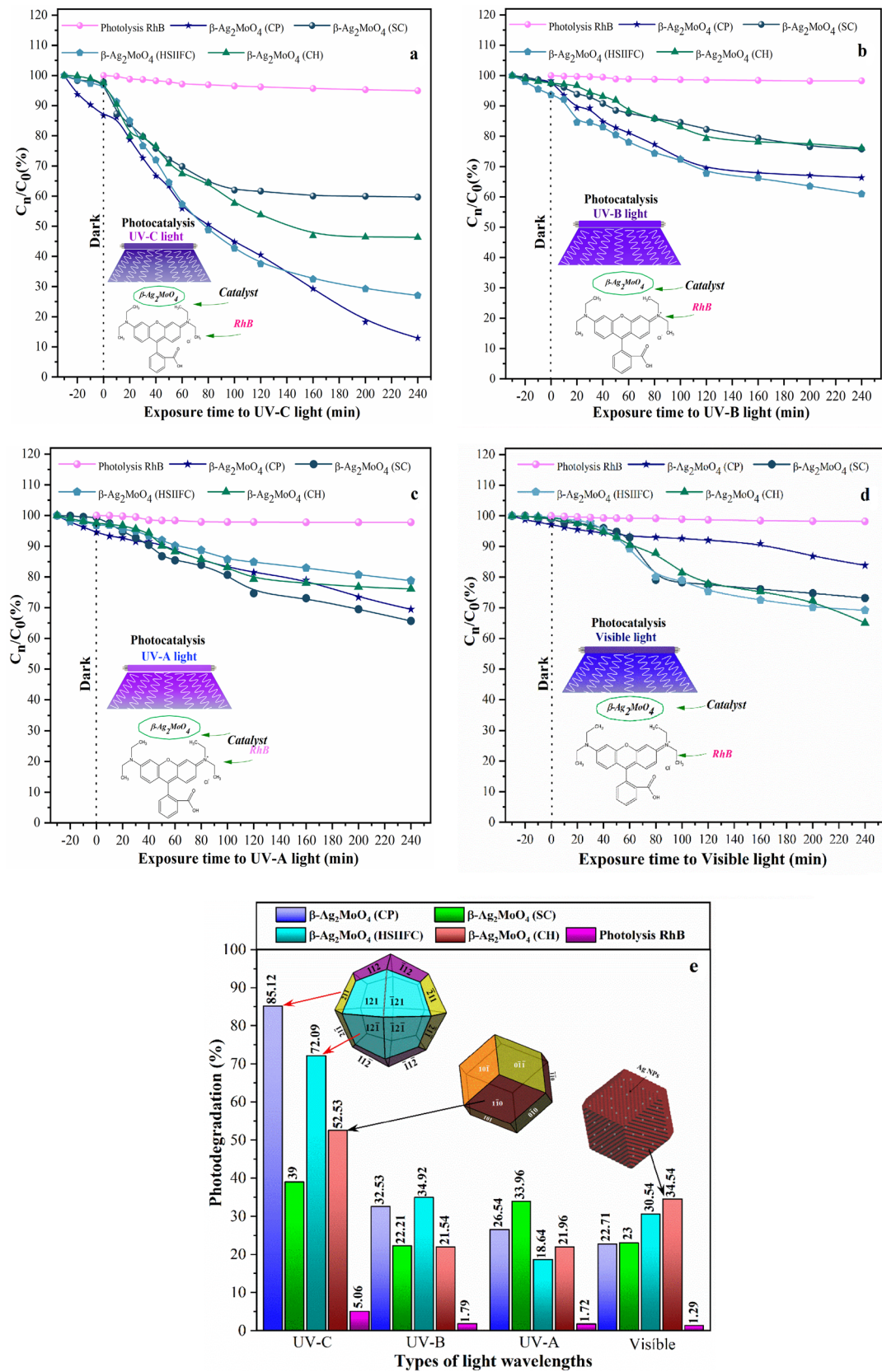


Fig. 10 a–e: Relative decay curves of the RhB dye solution concentration over the time of photolysis and photocatalysis, using $\beta\text{-Ag}_2\text{MoO}_4$ microcrystals as a catalyst, exposed to **a** UV-C, **b** UV-B, **c** UV-A, **d** Vis-lights radiation and **e** degradation rate for these photocatalytic tests

possible to obtain different morphologies for β - Ag_2MoO_4 microcrystals, varying only in the preparation form: irregular polyhedral (CP and CH), coat shape (SC), and an undefined morphology for the HSIIFC method. The UV–Vis analysis showed a maximum absorption in the UV region for all synthesized materials, located at approximately 280, 310, and 340 nm. However, β - Ag_2MoO_4 microcrystals made by the CH method still have a pronounced absorption band in the visible region, triggered by the formation of intermediate levels between VB and CB, arising from structural defects caused by the hydrothermal treatment, whereas the E_{gap} values for microcrystals prepared by CP, SC, HSIIFC and CH methods were as follows: 3.3; 3.27; 3.26 and 3.25 eV, respectively. Furthermore, the use of these routes also made it possible to prepare materials with different colors, which were confirmed and quantified by colorimetric analysis, suggesting a potential application of β - Ag_2MoO_4 microcrystals as inorganic pigments; the colors detected were as follows: Zinc Luster, Nile Clay, Gray (Crayola), and Charcoal Brown. From the DTF calculations it was possible to modulated all exposed surfaces observed experimentally by the FE-SEM technique of the β - Ag_2MoO_4 microcrystals, and, in association with the Wulff construction, these morphologies were achieved theoretically. The results suggest that the morphology composed only by the (112) surface should be more reactive due to its highest E_{pol} value, in which was confirmed by the photocatalytic tests. Finally, among the catalysts tested in photocatalytic assays for the degradation of the RhB dye solution, under exposure to different types of UV-lights and Vis-light illuminations, those made by the CP method showed the most promising results, particularly in the system composed of UV-C lamps, obtaining a discoloration rate of 85.12%, followed by microcrystals made by the methods of HSIIFC (72.09%), CH (52.53%) and SC (39%). These better degradation rate results were mainly attributed to the type of morphology of the microcrystals (24-phase trapezohedron), composed by the (112) surfaces which present a density of defects higher than the other surfaces with different kinds of Ag clusters with oxygen vacancies [$\text{AgO}_x \cdot 6 - x\text{V}_\text{O}$]. This fact allowed a greater reaction of the crystals with the pollutant and thus promoted its degradation.

Acknowledgements The authors thank CAPES, CNP, and FAPESP for their financial support, UFG-CRTI for the FE-SEM analyses, UFPI-LIMAV, UFPI-FISMAT, GERATEC-UESPI, to CETEM and PET-Chemistry UESPI for technical support. A.F.G. acknowledges the Generalitat Valenciana (Conselleria de Innovaci3n, Universidades, Ciencia y Sociedad Digital) for the postdoctoral contract (CIAPOS/2021/106).

Author Contributions This manuscript was written through the contributions of all authors that agreed with this submission. FHPL, LFGN, PBdeS, VEMV, KRBSC, and ACSJ prepared the samples and performed the UV–Vis measurements and photocatalytic assays. FHPL

and LSC performed the Rietveld refinement and structural analysis. KRBSC performed the Raman, and FT-IR measurements. YLO performed colorimetric measurements. MAPA, AFG, and LSC conceived the project. All authors participated in writing the manuscript and discussing all the results.

Funding The authors do have not any funding to pay for open access.

Data Availability The data that support the findings of this study are available on request from the corresponding author.

Declarations

Conflict of interest The authors declare that they have no conflict of interest.

References

1. K. Maeda, F. Takeiri, G. Kobayashi, S. Matsuishi, H. Ogino, S. Ida, T. Mori, Y. Uchimoto, S. Tanabe, T. Hasegawa, N. Imanaka, H. Kageyama, *Bull. Chem. Soc. Jpn.* (2022). <https://doi.org/10.1246/bcsj.20210351>
2. M. Humayun, H. Ullah, M. Usman, A. Habibi-Yangjeh, A. Ali Tahir, C. Wang, W. Luo, *J. Energy Chem.* (2022). <https://doi.org/10.1016/j.jechem.2021.08.023>
3. Q. Han, *Chem. Eng. J.* (2021). <https://doi.org/10.1016/j.cej.2020.127877>
4. X. Lang, S. Gopalan, W. Fu, S. Ramakrishna, *Bull. Chem. Soc. Jpn.* (2022). <https://doi.org/10.1246/bcsj.20200175>
5. K. Ariga, *Nanoscale Horiz.* (2021). <https://doi.org/10.1039/D0NH00680G>
6. Y. Ding, Y. Wan, Y.L. Min, W. Zhang, S.H. Yu, *Inorg. Chem.* (2008). <https://doi.org/10.1021/ic8007975>
7. X. Yu, T.J. Marks, A. Facchetti, *Nature Mater.* (2016). <https://doi.org/10.1038/nmat4599>
8. B. Saravanakumar, S.P. Ramachandran, G. Ravi, V. Ganesh, A. Sakunthala, R. Yuvakkumar, *Appl. Phys. A.* (2019). <https://doi.org/10.1007/s00339-018-2309-7>
9. B.J. Reddy, P. Vickraman, A.S. Justin, *Phys. Status Solidi A.* (2019). <https://doi.org/10.1002/pssa.201800595>
10. W. Ye, Y. Jiang, Q. Liu, D. Xu, E. Zhang, X.W. Cheng, Z. Wan, C. Liu, *J. Alloys Compd.* (2022). <https://doi.org/10.1016/j.jallcom.2021.161898>
11. R.M. Abdelhameed, M. Abu-Elghait, M. El-Shahat, J. Photochem. Photobiol. A. (2022). <https://doi.org/10.1016/j.jallcom.2021.161898>
12. E.A.C. Ferreira, N.F. Andrade Neto, A.A.G. Santiago, C.A. Paskocimas, M.R.D. Bomio, F.V. Motta, J. Mater. Sci. Mater. Electron. (2020). <https://doi.org/10.1007/s10854-020-02980-0>
13. Y.V.B. de Santana, J.E.C. Gomes, L. Matos, G.H. Cruvinel, A. Perrin, C. Perrin, J. Andr3s, J.A. Varela, E. Longo, *Nanomater. Nanotechnol.* (2014). <https://doi.org/10.5772/5893>
14. B.N.A. da Silva Pimentel, F.H. Marin-Dett, M. Assis, P.A. Barbugli, E. Longo, C.E. Vergani, *Front. Bioeng. Biotechnol.* (2022). <https://doi.org/10.3389/fbioe.2022.826123>
15. G.S. Sousa, F.X. Nobre, M.V.B. do Nascimento, O.C. Mendes, L. Manzato, Y.L. Ruiz, W.R. Brito, P.R.C. Couceiro, J.M.E. de Matos, *Inorg. Chem.* (2022). <https://doi.org/10.1021/acs.inorgchem.1c03245>
16. Y. Lian, Y. Wang, D. Zhang, L. Xu, *Colloids Surf. A* (2022). <https://doi.org/10.1016/j.colsurfa.2022.128348>

- 1211 17. L.H. da S Lacerda, E. Longo, J. Andrés, M.A. San-Miguel, J. Solid State Chem. (2022). <https://doi.org/10.1016/j.jssc.2021.122670>
- 1212
- 1213 18. S.C. Abrahams, J.M. Reddy, J. Chem. Phys. (1965). <https://doi.org/10.1063/1.1697153>
- 1214
- 1215 19. Y.P. Yadava, R.A. Singh, J. Mater. Sci. (1986). <https://doi.org/10.1007/BF00551496>
- 1216
- 1217 20. G.W. Smith, J.A. Ibers, Acta Crystallogr. (1965). <https://doi.org/10.1107/S0365110X65003201>
- 1218
- 1219 21. M. Théodet, C. Quilfen, C. Martínez, C. Aymonier, J. Supercrit. Fluids. (2016). <https://doi.org/10.1016/j.supflu.2016.07.002>
- 1220
- 1221 22. L.S. Cavalcante, E. Moraes, M.A.P. Almeida, C.J. Dalmaschio, N.C. Batista, J.A. Varela, E. Longo, M. Siu Li, J. Andrés, A. Beltrán, Polyhedron (2013). <https://doi.org/10.1016/j.poly.2013.02.006>
- 1222
- 1223 23. E.L.S. Souza, J.C. Sczancoski, I.C. Nogueira, M.A.P. Almeida, M.O. Orlandi, M.S. Li, R.A.S. Luz, M.G.R. Filho, E. Longo, L.S. Cavalcante, Ultrason. Sonochem. (2017). <https://doi.org/10.1016/j.ultrasonch.2017.03.007>
- 1224
- 1225 24. R.W.G. Wyckoff, J. Am. Chem. Soc. (1922). <https://doi.org/10.1021/ja01430a017>
- 1226
- 1227 25. F. Rocca, A. Kuzmin, P. Mustarelli, C. Tomasi, A. Magistris, Solid State Ionics (1999). [https://doi.org/10.1016/S0167-2738\(98\)00546-3](https://doi.org/10.1016/S0167-2738(98)00546-3)
- 1228
- 1229 26. N. Senguttuvan, S.M. Babu, C. Subramanian, Mater. Eng. B Sci. (1997). [https://doi.org/10.1016/S0921-5107\(97\)00039-1](https://doi.org/10.1016/S0921-5107(97)00039-1)
- 1230
- 1231 27. R.H.N. Frazão, D.G.D. Rocca, S.M. de Amorim, R.A. Peralta, C.D. Moura-Nickel, A. de Noni, R.F.P.M. Moreira, Environ. Technol. (2019). <https://doi.org/10.1080/09593330.2019.1663939>
- 1232
- 1233 28. Y. Chen, X. Xie, Y. Si, P. Wang, Q. Yan, Appl. Surf. Sci. (2019). <https://doi.org/10.1016/j.apsusc.2019.143860>
- 1234
- 1235 29. F.H.P. Lopes, L.F.G. Noleto, V.E.M. Vieira, A.C.S. Jucá, K.R.B. da S, M.S. de Costa, P.B. de Oliveira, Y.L. de Sousa, G.O. de Oliveira, M. Gusmão, *Química: Debate Entre a Vida Moderna e o Meio Ambiente* (EditoraAtena, Chennai, 2021), pp.150–164. <https://doi.org/10.22533/at.ed.783211204>
- 1236
- 1237 30. F.S. Cunha, F.H.P. Lopes, A.C.S. Jucá et al., *Estudos Interdisciplinares Nas Ciências Exatas e Da Terra e Engenharias* (Chennai, Editora Atena, 2019), pp.300–324. <https://doi.org/10.22533/at.ed.423192309>
- 1238
- 1239 31. G.S. Sousa, F.X. Nobre, E.A. Araújo Júnior, J.R. Sambrano, A.R. Albuquerque, R.S. Bindá, P.R.C. Couceiro, W.R. Brito, L.S. Cavalcante, M.R.M.C. Santos, J.M.E. de Matos, Arabian J. Chem (2020). <https://doi.org/10.1016/j.arabjc.2018.07.011>
- 1240
- 1241 32. J.V.B. Moura, T.S. Freitas, R.P. Cruz, R.L.S. Pereira, A.R.P. Silva, A.T.L. Santos, J.H. da Silva, C. Luz-Lima, P.T.C. Freire, H.D.M. Coutinho, Biomed. Pharmacother. (2017). <https://doi.org/10.1016/j.biopha.2016.12.016>
- 1242
- 1243 33. N.F. Andrade Neto, A.B. Lima, M.R.D. Bomio, F.V. Motta, J. Alloys Compd. (2020). <https://doi.org/10.1016/j.jallcom.2020.156077>
- 1244
- 1245 34. D.W.R. Coimbra, F.S. Cunha, J.C. Sczancoski, J.F.S. de Carvalho, F.R.C. de Macêdo, L.S. Cavalcante, J. Mater. Sci.: Mater. Electron. (2019). <https://doi.org/10.1007/s10854-018-0401-6>
- 1246
- 1247 35. A. Beltrán, L. Gracia, E. Longo, J. Andrés, J. Phys. Chem. C. (2014). <https://doi.org/10.1021/jp4118024>
- 1248
- 1249 36. V. Teodoro, A.F. Gouveia, T.R. Machado, A.B. Trench, N. Jacomaci, M. Assis, Ceram. Int. (2022). <https://doi.org/10.1016/j.ceramint.2021.10.156>
- 1250
- 1251 37. C.H.B. Ng, W.Y. Fan, Cryst. Growth Des. (2015). <https://doi.org/10.1021/acs.cgd.5b00455>
- 1252
- 1253 38. C.A. Oliveira, D.P. Volanti, A.E. Nogueira, C.A. Zamperini, C.E. Vergani, E. Longo, Mater. Des. (2017). <https://doi.org/10.1016/j.matdes.2016.11.032>
- 1254
- 1255 39. M.T. Fabbro, C.C. Foggi, L.P.S. Santos, L. Gracia, A. Perrin, C. Perrin, C.E. Vergani, A.L. Machado, J. Andrés, E. Cordoncillo, E. Longo, Dalton Trans. (2016). <https://doi.org/10.1039/C6DT00343E>
- 1256
- 1257 40. E.A.C. Ferreira, N.F. Andrade Neto, M.R.D. Bomio, F.V. Motta, Ceram. Int. (2019). <https://doi.org/10.1016/j.ceramint.2019.03.012>
- 1258
- 1259 41. F.C. Fraga, D.G.D. Rocca, H.J. Joséa, H.F.V. Victória, J.B.G. Filho, K. Krambrock, E. Rodríguez-Castellón, R.F.P.M. Moreira, J. Photochem. Photobiol. A. (2022). <https://doi.org/10.1016/j.jphotochem.2022.114102>
- 1260
- 1261 42. Y.L. Oliveira, M.J.S. Costa, A.C.S. Jucá, L.K.R. Silva, E. Longo, N.S. Arul, L.S. Cavalcante, J. Mol. Struct. (2020). <https://doi.org/10.1016/j.molstruc.2020.128774>
- 1262
- 1263 43. Y.L. Oliveira, A.F. Gouveia, M.J.S. Costa, F.H.P. Lopes, J.C. Sczancoski, E. Longo, G.E. Luz, R.S. Santos, L.S. Cavalcante, Mater. Sci. Energy Technol. (2022). <https://doi.org/10.1016/j.mset.2021.12.006>
- 1264
- 1265 44. H.M. Rietveld, J. Appl. Crystallogr. (1969). <https://doi.org/10.1107/S0021889869006558>
- 1266
- 1267 45. M. Bortolotti, L. Lutterotti, I. Lonardelli, J. Appl. Cryst. (2009). <https://doi.org/10.1107/S0021889809008309>
- 1268
- 1269 46. K. Momma, F. Izumi, J. Appl. Cryst. (2008). <https://doi.org/10.1107/S0021889808012016>
- 1270
- 1271 47. K. McLAREN, J. Soc. Dyers Colour. (1976). <https://doi.org/10.1111/j.1478-4408.1976.tb03301.x>
- 1272
- 1273 48. R. McDonald, K.J. Smith, J. Soc. Dyers Colour. (1995). <https://doi.org/10.1111/j.1478-4408.1995.tb01688.x>
- 1274
- 1275 49. J.P. Perdew, K. Burke, M. Ernzerhof, Phys. Rev. Lett. (1996). <https://doi.org/10.1103/physrevlett.77.3865>
- 1276
- 1277 50. J.P. Perdew, J.A. Chevary, S.H. Vosko, K.A. Jackson, M.R. Pederson, D.J. Singh, C. Fiolhais, Phys. Rev. B. (1992). <https://doi.org/10.1103/PhysRevB.46.6671>
- 1278
- 1279 51. G. Kresse, J. Furthmüller, Phys. Rev. B - Condens. Matter Mater. Phys. (1996). <https://doi.org/10.1103/PhysRevB.54.11169>
- 1280
- 1281 52. G. Kresse, J. Hafner, Phys. Rev. B **49**, 14251 (1994). <https://doi.org/10.1103/PhysRevB.49.14251>
- 1282
- 1283 53. V. Teodoro, A.F. Gouveia, T.R. Machado, A.B. Trench, N. Jacomaci, M. Assis, G.E. Marques, M.D. Teodoro, M.A. San-Miguel, J. Andrés, J. Bettini, E. Longo, Ceram. Int. **48**, 3 (2022). <https://doi.org/10.1016/j.ceramint.2021.10.156>
- 1284
- 1285 54. J. Andrés, L. Gracia, A.F. Gouveia, M.M. Ferrer, E. Longo, Nanotechnology (2015). <https://doi.org/10.1088/0957-4484/26/40/405703>
- 1286
- 1287 55. G.D. Barmparis, Z. Lodziana, N. Lopez, I.N. Remediakis, Beilstein J. Nanotechnol. (2015). <https://doi.org/10.3762/bjnano.6.35>
- 1288
- 1289 56. G.Z. Wulff, Krystallog. (1901). <https://doi.org/10.1524/zkri.1901.34.1.449>
- 1290
- 1291 57. N.G. Macedo, A.F. Gouveia, R.A. Roca, M. Assis, L. Gracia, J. Andrés, E.R. Leite, E. Longo, J. Phys. Chem. C. (2018). <https://doi.org/10.1021/acs.jpcc.8b01898>
- 1292
- 1293 58. N. Pachauri, G.B.V.S. Lakshmi, S. Sri, P.K. Gupta, P.R. Solanki, Mater. Sci. Eng. C. (2020). <https://doi.org/10.1016/j.msec.2020.110911>
- 1294
- 1295 59. F.S. Cunha, J.C. Sczancoski, I.C. Nogueira, V.G. de Oliveira, S.M.C. Lustosa, E. Longo, L.S. Cavalcante, CrystEngComm (2015). <https://doi.org/10.1039/C5CE01662B>
- 1296
- 1297 60. B.H. Toby, Powder Diffr. (2006). <https://doi.org/10.1154/1.2179804>
- 1298
- 1299 61. A. Zareie-Darmian, H. Farsi, A. Farrokhi, R. Sarhaddi, Z. Li, Phys. Chem. Chem. Phys. (2021). <https://doi.org/10.1039/D0CP05673A>
- 1300
- 1301 62. G.S. Sousa, F.X. Nobre, E.A.A. Júnior, R.D.S. Bezerra, M.L. de Sá, J.M.E. de Matos, M.R.M.C. Santos, Environ. Nanotechnol. 1340

- 1342 Monit Manage. (2020). <https://doi.org/10.1016/j.enmm.2020.100379>
- 1343
- 1344 63. K. Momma, F. Izumi, J. Appl. Cryst. (2011). <https://doi.org/10.1107/S0021889811038970>
- 1345
- 1346 64. A.F. Gouveia, J.C. Sczancoski, M.M. Ferrer, A.S. Lima, M.R.M.C. Santos, M.S. Li, R.S. Santos, E. Longo, L.S. Cavalcante, Inorg. Chem. (2014). <https://doi.org/10.1021/ic500335x>
- 1347
- 1348 65. J.V.B. Moura, J.G. da Silva Filho, P.T.C. Freire, C. Luz-Lima, G.S. Pinheiro, B.C. Viana, J. Mendes Filho, A.G. Souza-Filho, G.D. Saraiva, Vib. Spectrosc. (2016). <https://doi.org/10.1016/j.vibspec.2016.06.009>
- 1349
- 1350 66. P.B. Almeida, I.M. Pinatti, R.C. de Oliveira, M.M. Teixeira, C.C. Santos, T.R. Machado, E. Longo, I.L.V. Rosa, Chem. Pap. (2021). <https://doi.org/10.1007/s11696-020-01489-4>
- 1351
- 1352 67. M.T. Fabbro, C. Saliby, L.R. Rios, F.A. La Porta, L. Gracia, M.S. Li, J. Andrés, L.P.S. Santos, E. Longo, Sci. Adv. Mater. Technol. (2015). <https://doi.org/10.1088/1468-6996/16/6/065002>
- 1353
- 1354 68. J. Li, F. Liu, Y. Li, New J. Chem. (2018). <https://doi.org/10.1039/C8NJ02327A>
- 1355
- 1356 69. Y. Song, W. Xie, C. Yang, D. Wei, X. Su, L. Li, L. Wang, J. Wang, J. Mater. Res. Technol. (2020). <https://doi.org/10.1016/j.jmrt.2020.03.102>
- 1357
- 1358 70. L.S. Cavalcante, J.C. Sczancoski, N.C. Batista, E. Longo, J.A. Varela, M.O. Orlandi, Adva. Powder Technol. (2013). <https://doi.org/10.1016/j.apt.2012.08.007>
- 1359
- 1360 71. J. Andrés, M.M. Ferrer, L. Gracia, A. Beltran, V.M. Longo, G.H. Cruvinel, R.L. Tranquilin, E. Longo, Part. Part. Syst. Charact. (2019). <https://doi.org/10.1002/ppsc.201400162>
- 1361
- 1362 72. KrystalShaper (2018) <http://www.jcrystal.com/products/krystalshaper/>
- 1363
- 1364 73. P. Kubelka, F. Munk, Z. Tech, Phys. **12**, 593 (1931)
- 1365
- 1366 74. A.B. Murphy, J. Phys. D: Appl. Phys. (2006). <https://doi.org/10.1088/0022-3727/39/16/008>
- 1367
- 1368 75. L. Yang, B. Kruse, J. Opt. Soc. Am. A (2004). <https://doi.org/10.1364/JOSAA.21.001933>
- 1369
- 1370 76. R. Lacombe-Perales, J. Ruiz-Fuertes, D. Errandonea, D. Martínez-García, A. Segura, EPL (2008). <https://doi.org/10.1209/0295-5075/83/37002>
- 1371
- 1372 77. H. Jiang, J.-K. Liu, J.-D. Wang, Y. Lu, X.-H. Yang, CrystEngComm (2015). <https://doi.org/10.1039/C5CE00039D>
- 1373
- 1374 78. S. Balasurya, A. Syed, L.L. Raju, S. Al-Rashed, A.M. Thomas, A. Das, S.S. Khan, Opt. Mater. (2021). <https://doi.org/10.1016/j.optmat.2021.110856>
- 1375
- 1376 79. G. Matafonova, V. Batoev, Water Res. (2018). <https://doi.org/10.1016/j.watres.2017.12.079>
- 1377
- 1378 80. X. Li, Y. Wang, Z. Pan, Ceram. Int. (2019). <https://doi.org/10.1016/j.ceramint.2019.07.155>
- 1379
- 1380 81. J.C. Ragain, J. Dent. Oral Disord. Ther. (2016). <https://doi.org/10.15226/jdodt.2016.00148>
- 1381
- 1382 82. X. Zhao, Y. Zhang, Y. Huang, H. Gong, J. Zhao, Dyes Pigment. (2015). <https://doi.org/10.1016/j.dyepig.2015.01.018>
- 1383
- 1384 83. M.A. Patel, B.A. Bhanvase, S.H. Sonawane, Ultrason. Sonochem. (2013). <https://doi.org/10.1016/j.ultsonch.2012.11.008>
- 1385
- 1386 84. H.S. Cha, B. Yu, Y.K. Lee, J. Adv. Prosthodont. (2013). <https://doi.org/10.4047/jap.2013.5.3.262>
- 1387
- 1388 85. F.H. Alhamedi, M.A. Rauf, Desalin. (2009). <https://doi.org/10.1016/j.desal.2008.03.016>
- 1389
- 1390 86. Z.L. Ye, C.Q. Cao, J.C. He, R.X. Zhang, H.Q. Hou, Chinese Chem. Lett. (2009). <https://doi.org/10.1016/j.ccllet.2008.12.033>
- 1391
- 1392 87. M.A. Saidani, A. Fkiri, L.-S. Smiri, J. Inorg. Organomet. Polym. (2019). <https://doi.org/10.1007/s10904-019-01075-6>
- 1393
- 1394 88. F. Wu, F. Chang, J. Zheng, M. Jiao, B. Deng, X. Hu, X. Liu, J. Inorg. Organomet. Polym. (2018). <https://doi.org/10.1007/s10904-017-0731-5>
- 1395
- 1396 89. A. Bilgic, J. Alloys Compd. (2022). <https://doi.org/10.1016/j.jallcom.2021.163360>
- 1397
- 1398 90. M. Yan, Y. Wu, F. Zhu, Y. Hua, W. Shi, Phys. Chem. Chem. Phys. (2016). <https://doi.org/10.1039/C5CP05599G>
- 1399
- 1400
- 1401
- 1402
- 1403
- 1404
- 1405
- 1406
- 1407
- 1408
- 1409
- 1410 **Publisher's Note** Springer Nature remains neutral with regard to jurisdictional claims in published maps and institutional affiliations.
- 1411
- 1412 Springer Nature or its licensor (e.g. a society or other partner) holds exclusive rights to this article under a publishing agreement with the author(s) or other rightsholder(s); author self-archiving of the accepted manuscript version of this article is solely governed by the terms of such publishing agreement and applicable law.
- 1413
- 1414
- 1415
- 1416

Journal:	10904
Article:	2509

Author Query Form

Please ensure you fill out your response to the queries raised below and return this form along with your corrections

Dear Author

During the process of typesetting your article, the following queries have arisen. Please check your typeset proof carefully against the queries listed below and mark the necessary changes either directly on the proof/online grid or in the 'Author's response' area provided below

Query	Details Required	Author's Response
AQ1	Kindly check and confirm whether the processed Figures is correctly identified.	
AQ2	Please check the layout of Table(s) 1, 4, and correct if necessary.	
AQ3	As per the information provided by the publisher, Table 5 and figure 9 will be black and white in print; hence, please confirm whether we can add "colour figure online" to the caption.	
AQ4	Reference [43, 63, 75] was provided in the reference list; however, this was not mentioned or cited in the manuscript. As a rule, if a citation is present in the text, then it should be present in the list. Please provide the location of where to insert the reference citation in the main body text. Kindly ensure that all references are cited in ascending numerical order.	